The high-resolution three-dimensional solution structures of the oxidized and reduced states of human thioredoxin

Jun Qin, G Marius Clore* and Angela M Gronenborn*

Laboratory of Chemical Physics, Building 5, National Institute of Diabetes and
Digestive and Kidney Diseases, National Institutes of Health, Bethesda, MD 20892, USA

Background: Thioredoxin is a ubiquitous protein and is involved in a variety of fundamental biological functions. Its active site is conserved and has two redox active cysteines in the sequence Trp-Cys-Gly-Pro-Cys. No structures of the oxidized and reduced states from the same species have been determined at high resolution under the same conditions and using the same methods. Hence, any detailed comparison of the two oxidation states has been previously precluded.

Results: The reduced and oxidized states of the (C62A, C69A, C73A) mutant of human thioredoxin have been investigated by multidimensional heteronuclear NMR. Structures for both states were determined on the basis of approximately 28 experimental restraints per residue, and the resulting precision of the two structures is very high. Consequently, subtle differences between the

oxidized and reduced states can be reliably assessed and evaluated. Small differences, particularly within and around the active site can be discerned.

Conclusions: Overall, the structures of the reduced and oxidized states of the (C62A, C69A, C73A) mutant of human thioredoxin are very similar (with a backbone atomic root mean square difference of about 0.9 Å) and the packing of side chains within the protein core is nearly identical. The conformational change between oxidized and reduced human thioredoxin is very small and localized to areas in spatial proximity to the redox active cysteines. These subtle structural differences, in addition to the restriction of conformational freedom within the active site upon oxidation, may be important for the different activities of thioredoxin involving a variety of target proteins.

Introduction

Thioredoxin is a ubiquitous dithiol oxidoreductase found in many organisms and involved in numerous biochemical processes [1,2]. Although the most widely studied thioredoxin is from *Escherichia coli*, thioredoxins from other bacteria, bacteriophages, plants, and mammals have also been isolated and sequenced, and have been found to exhibit between 25 and 70 % sequence identity with *E. coli* thioredoxin [3]. Thioredoxin activity is related to the thiol–disulfide redox chemistry of two cysteine residues found in the conserved active site sequence Trp-Cys-Gly-Pro-Cys which is present in all species [1,2]. Thioredoxin acts as a hydrogen donor for reductive enzymes such as ribonucleotide reductase [4,5]; functions as a general reductant for disulfides in proteins including insulin, oxytocin, and fibrinogen [1]; and serves as a regulatory factor for enzymes or receptors in photosynthetic systems [6]. Specific activities associated with human thioredoxin include the induction of interleukin-2 receptor expression [7], autocrine growth factor properties [8], and the stimulation of the DNA-binding activity of the transcription factor NF-κB [9,10].

The mechanism of the redox-related functions of *E. coli* thioredoxin has been proposed to involve nucleophilic attack by the more reactive Cys32 thiolate anion on a disulfide-containing substrate, producing a mixed-disulfide intermediate, which is then attacked by the

thiolate of Cys35 to yield a reduced substrate and free, oxidized thioredoxin [11]. A number of experimental measurements including fluorescence [12], NMR [13–15], hydrogen exchange [16], specific volume and adiabatic compressibility [17] have indicated that there are subtle conformational differences between the oxidized and reduced states of thioredoxin, the nature of which have not yet been characterized.

E. coli thioredoxin also has several non-redox related functions. For example, it constitutes an essential subunit in the phage T7 DNA polymerase and is required in the assembly of filamentous phages [18,19]. These activities are associated with the reduced protein, and it has been established that the redox cycle is not required since mutants of thioredoxin with one or both active site cysteines replaced by serine or alanine are also active [19]. Subtle structural and dynamic differences between the reduced and oxidized forms have been invoked to explain these functional changes [20]. Mutagenesis studies indicate that the conserved active site region plays an important role in interacting with other proteins for both redox and non-redox related functions of thioredoxin [18,19,21–24]. In contrast to our extensive knowledge about *E. coli* thioredoxin, little is known about the functional activities of human thioredoxin beyond its general redox properties.

The three-dimensional structures of a number of different thioredoxins have been determined, with the

*Corresponding authors.

aim of shedding light on the catalytic mechanism of thioredoxin. These include the structure of oxidized *E. coli* thioredoxin by X-ray crystallography [25,26], and the solution structures of reduced *E. coli* [27] and human [28] thioredoxins determined by two-dimensional NMR. The *E. coli* and human proteins exhibit very similar three-dimensional folds despite the large variation in amino acid sequence (25 % sequence identity with some deletions and insertions). However, none of the structures were determined at high resolution under the same conditions and using the same methods for both the reduced and oxidized states of thioredoxin from the same species. Hence, any detailed comparisons of the oxidized and reduced states is precluded, particularly as the structural differences are clearly very subtle in nature. Moreover, the precision and accuracy of the two previous NMR structure determinations of reduced *E. coli* [27] and human [28] thioredoxins would be insufficient to permit the detection of minor changes between the reduced and oxidized states.

Clearly, a detailed structural comparison between reduced and oxidized forms of human thioredoxin will be of considerable importance for understanding the functional properties of human thioredoxin and of thioredoxins in general. The comparison may also shed light on the structural role of the reduced state of thioredoxin for its non-redox related function.

In this paper we present high-resolution three-dimensional structures of the reduced and oxidized states of the triple Cys →Ala mutant (C62A, C69A, C73A) of human thioredoxin in solution using multidimensional heteronuclear NMR spectroscopy. This mutant, rather than the wild-type protein, was chosen for study in order to circumvent any problems arising from inter-molecular disulfide bond formation by the three free non-active site cysteine residues upon oxidation. Previous studies have shown that this mutant has virtually the same activity as the wild-type protein and that the structures of the mutant and wild-type proteins are essentially indistinguishable [29]. The present structures have been determined on the basis of about 28 experimental restraints per residue. As a result, the precision with which the coordinates have been determined is very high, namely 0.18–0.19 Å for the backbone atoms, 0.58–0.60 Å for all atoms, and 0.30–0.31 Å for all atoms of residues which do not exhibit conformational disorder in solution. This represents an approximately 50 % increase in the number of nuclear Overhauser enhancement (NOE) derived interproton distance restraints, a 120 % increase in the backbone precision and a 70 % increase in the precison of ordered side chains relative to our previous structure determination of wild-type reduced human thioredoxin [28]. As a result, subtle differences between the oxidized and reduced states can be observed with great confidence. We show that while the global fold is extremely similar between the reduced and oxidized forms of human thioredoxin,

there exist some important localized conformational differences particularly in the active site region.

Results and discussion

The converged structures

With the exception of interproton distance restraints between NH protons which were derived from a three-dimensional (3D) ^{15}N-separated NOE spectrum [30,31], all the interproton distance restraints were derived from 4D ^{15}N/^{13}C-separated and ^{13}C/^{13}C-separated NOE spectra [32–34]. In the 4D ^{15}N/^{13}C-separated spectrum, through-space interactions between NH protons and carbon-attached protons are observed, while in the 4D ^{13}C/^{13}C-separated spectrum the through-space interactions involve only carbon-attached protons. Examples of the quality of the 4D heteronuclear-separated spectra are shown in Fig. 1. The final sets of 40 simulated annealing structures for the reduced and oxidized states of the (C62A, C69A, C73A) mutant of human thioredoxin were based on 2933 and 3018 experimental NMR restraints, respectively. For the reduced structures, these comprise 2571 approximate interproton distance restraints, 273 torsion angle restraints and 89 $^3J_{HN\alpha}$ coupling constant restraints. For the oxidized structures, these comprise 2649 approximate interproton distance restraints, 278 torsion angle restraints and 91 $^3J_{HN\alpha}$ coupling constant restraints. As in all structure determinations from our laboratory [35], the NOE-derived interproton distance restraints are treated in a very conservative manner and are simply classified into four distance ranges: 1.8–2.7 Å (1.8–2.9 Å for NOEs involving NH protons), 1.8–3.3 Å (1.8–3.5 Å for NOEs involving NH protons), 1.8–5.0 Å and 1.8–6.0 Å, corresponding to strong, medium, weak and very weak NOEs, respectively [36,37]. In addition, stereospecific assignments were obtained for 51 out of the 69 β-methylene groups, and for all methyl groups of the 6 leucine and 11 valine residues. Thus, the average number of experimental NMR restraints per residue is 27.9 for the reduced state and 28.7 for the oxidized state. If one considers that the inter-residue NOE distance restraints affect two residues, while the intra-residue ones affect only one residue, there are an average of 42.0 and 43.7 experimental distance restraints affecting the conformation of each residue for the reduced and oxidized states, respectively. A summary of the distribution of NOEs per residue is shown in Fig. 2, and a plot of the backbone chemical shift differences between the two oxidation states is provided in Fig. 3. A summary of the structural statistics, and of the atomic root mean square (rms) differences and angular standard deviations of the backbone and side chain torsion angles is provided in Tables 1 and 2, respectively. Plots of the atomic and torsion angle rms deviations of the coordinates of the simulated annealing structures as a function of residue are provided in Figs 4a and 5b, respectively, and best fit superpositions of the en-

semble of structures are shown in Fig. 6. All the structures satisfy the NMR interproton distance, torsion angle and $^3J_{HN\alpha}$ coupling constant restraints within experimental error, display very small deviations from idealized covalent geometry, and exhibit good non-bonded contacts as exemplified by large negative values of the Lennard–Jones van der Waals energy (Table 1). There are no violations >0.3 Å for the interproton distance restraints or >3° for the torsion angle restraints, and there are no systematic interproton distance violations between 0.1 Å and 0.3 Å among the two ensembles of calculated structures. In addition, all the φ, ψ backbone torsion angles lie within the allowed regions of the Ramachandran plot. Specifically, excluding glycines, 80% of the residues lie in the most favored regions and 20% in the additional allowed regions of the Ramachandran plot as defined by the program PROCHECK [38].

As is evident from the data in Table 2 and Figs 4, 5 and 6, the structures are exceptionally well-determined with a backbone atomic precision of 0.19 Å and 0.18 Å for the reduced and oxidized states, respectively, and average φ and ψ angular rms deviations of about 1.5° and 3°, respectively. (Note that the precision of the coordinates is given by the value of the average atomic rms deviation of the individual structures in a given ensemble from the overall mean coordinate positions for the ensemble.) In addition, the precision for ordered side chains (0.3 Å) is only slightly higher than that for the backbone atoms. As a substantial number of the side chain atoms at the surface of the molecule are disordered, the precision of all atoms is clearly lower (~0.6 Å). A key aspect of being able to compare the structures of the reduced and oxidized states lies not only in the precision of the structures but, more importantly, in their accuracy. A recent detailed investigation of the factors affecting the precision and accuracy of NMR structures showed that the overall ratio of precision to accuracy for an ensemble of calculated structures remains fairly constant and, taking into account uncertainties arising from the representation of the non-bonded interactions, has a value of ~0.4 for backbone atoms, ~0.6 for all atoms and ~0.5 for all ordered atoms [39]. This translates into an estimated accuracy for the ensemble of calculated structures of ~0.5 Å for the backbone atoms, ~1.0 Å for all atoms and ~0.6 Å for all ordered atoms. However, the accuracy of the mean coordinates is always higher than that of the ensemble [39,40] and the ratio of the mean coordinate position accuracy to the ensemble accuracy is also approximately constant with values of ~0.8, ~0.6 and ~0.7 for backbone atoms, all atoms and all ordered atoms, respectively [39]. Thus, the estimated accuracy of the mean coordinates for the reduced and oxidized states is ~0.4 Å for the backbone atoms and all ordered atoms, and ~0.6 Å for all atoms.

An independent assessment of accuracy can be obtained by complete cross-validation [41]. To this end,

a series of simulated annealing calculations with complete cross-validation was carried out on the final sets of 40 structures for both the reduced and oxidized states. In these calculations, the experimental NOE restraints were randomly partitioned into a test set comprising ~10% of the data (which is left out of the target function) and a reference set. Because each NOE is specific to a pair of protons and because certain NOEs carry more structural information than others (for example, NOEs between residues far apart in the sequence compared with intra-residue or sequential NOEs), the test set is different for each structure calculation. By this means, it is possible to assess not only how well the omitted restraints in the test set are predicted by the remaining restraints in the reference set, but also how the omission of data affects the coordinate positions. The average rms deviation from the interproton distance bounds in the test data sets is 0.13 Å which is a factor of 10 higher than in the reference set and the average number of violations >0.5 Å (but <1.0 Å) for the test sets is 3.0 ± 1.7 and 3.1 ± 2.1 for the reduced and oxidized ensembles of cross-validated strcutures, respectively. (Note that the violations in the test sets invariably involve surface side chains.) These values are a factor of about two smaller than those for the high-resolution NMR structure of the immunoglobulin-binding domain of protein G [41] and demonstrate the high degree to which each interproton distance is predicted by the remaining ones. The precision of the ensemble of structures calculated with complete cross-validation relative to the structures calculated without it is unchanged for all atoms and only 20% lower for the backbone atoms. Moreover, the shift in the mean coordinate positions between the structures calculated before and after complete cross-validation is 0.08 Å for the backbone atoms of both the reduced and oxidized states, and 0.16 Å and 0.15 Å for all atoms of the reduced and oxidized states, respectively. Thus, the difference between the mean coordinate positions before and after complete cross-validation is significantly smaller than the precision of the ensemble of structures. These results indicate the high degree of completeness of the experimental data and provide a reliable indication of the accuracy of the structures.

The overall fold

The three-dimensional structure of the (C62A, C69A, C73A) mutant of human thioredoxin is clearly very similar to that of the wild-type protein. The backbone atomic rms differences between the mean structures of the reduced wild-type [28] and reduced mutant proteins and between the mean structures of the reduced wild-type and oxidized mutant proteins are 0.79 Å and 0.71 Å, respectively. Given the precision (0.4 Å) and consequent accuracy (~0.8 Å; [39]) of the mean backbone coordinate positions of the reduced wild-type protein [28], one can conclude that, within the errors of the coordinates of the wild-type protein, there is
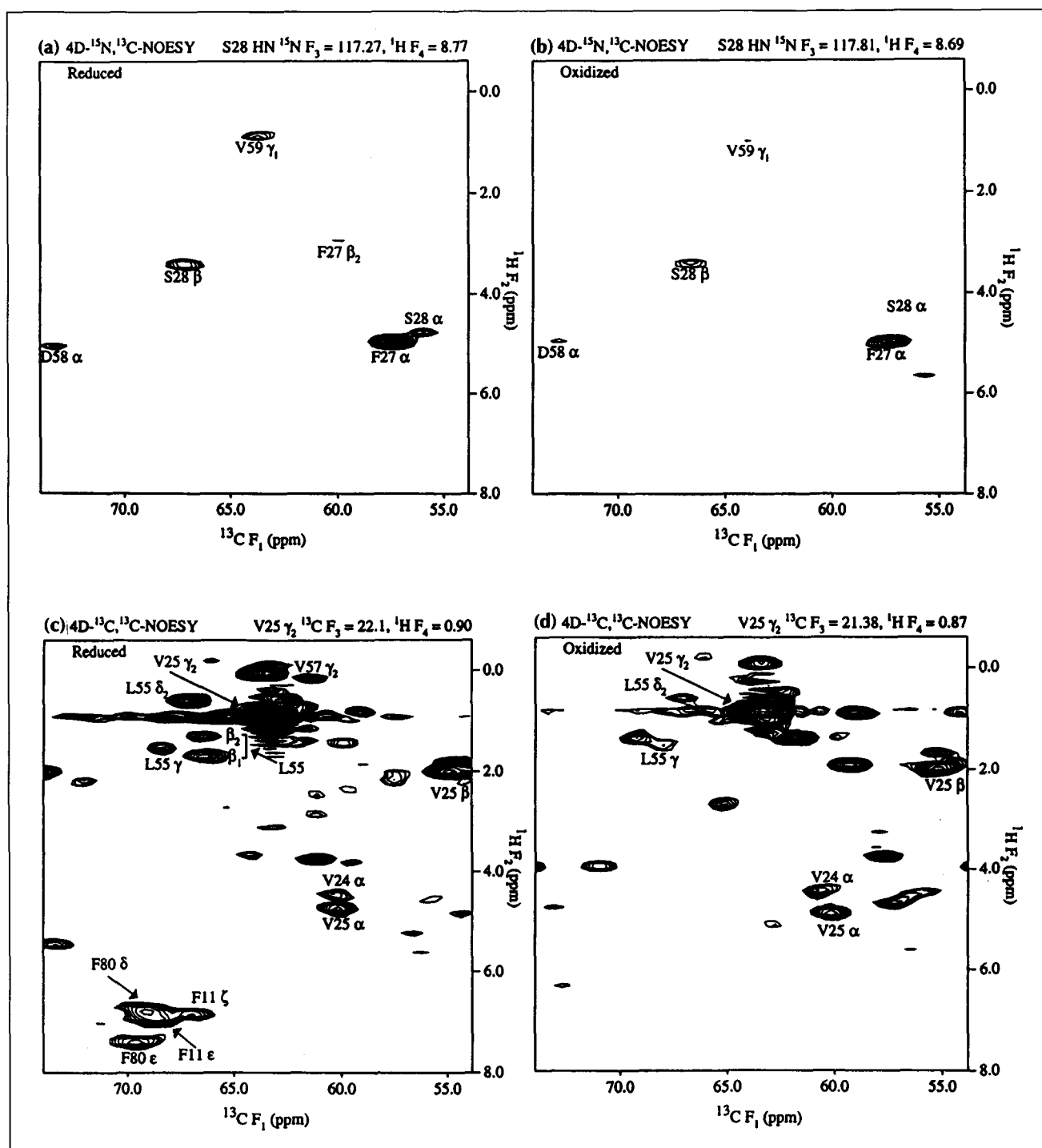
Fig. 1. Examples of **(a)**,**(b)** $^{13}C(F_1)-^1H(F_2)$ planes of the 4D $^{15}N/^{13}C$-separated NOE spectra and **(c)**,**(d)** 4D $^{13}C/^{13}C$-separated NOE spectra of the reduced and oxidized states of the (C62A, C69A, C73A) mutant of human thioredoxin. Spectra of reduced thioredoxin are shown in (a) and (c) and of oxidized thioredoxin in (b) and (d). The destination proton in (a) and (b) is the NH of Ser28 and in (c) and (d) is the $C^{\gamma2}H_3$ methyl group of Val25. Peaks that are not labeled in (c) and (d) have their maximum intensity in an adjacent plane and do not involve the $C^{\gamma2}H_3$ group of Val25.

no significant difference between the structures of the wild-type and mutant proteins. The structures of the human protein are also closely similar to those of the *E. coli* protein [26] exhibiting a backbone rms difference of 1.5–1.7 Å with 99 to 101 residues superimposed, as expected given their 25 % sequence identity.

The key question in understanding the enzymatic properties of thioredoxin concerns the differences between the oxidized and reduced protein. Spectroscopic studies of the *E. coli* protein [12] demonstrate a conformational change, but in order to assess the magnitude and pertinent features of this change, a com-
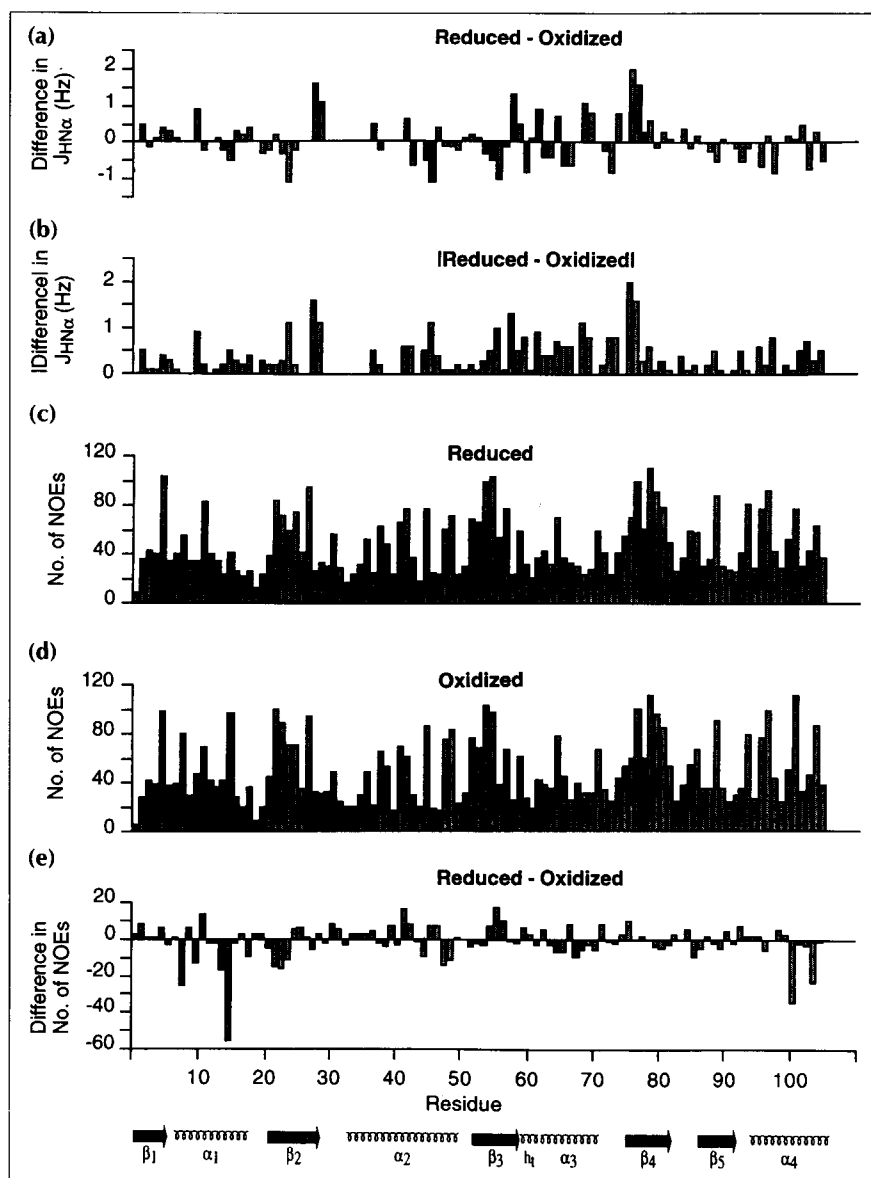
Fig. 2. Differences in (a),(b) measured $^3J_{HN\alpha}$ coupling constants, (c),(d) number of NOE restraints per residue, and (e) differences in number of NOE restraints between the reduced and oxidized states of the (C62A, C69A, C73A) mutant of human thioredoxin. A schematic illustration of the secondary structure is shown below the figure with α-helices depicted as coils and β-strands as arrows.

parison of high quality structures is necessary. The structures of the reduced and oxidized states of the (C62A, C69A, C73A) mutant of human thioredoxin are such structures, and, perhaps surprisingly, no major differences are apparent (Fig. 6). The structures comprise a five-stranded β-sheet (residues 1–5, 22–28, 53–59, 75–81 and 84–91) surrounded by four α-helices (residues 7–17, 33–49, 62–70 and 94–105) and a small helical turn (residues 58–62). The five strands are arranged in a $-2x$, $+1x$, -2, -1 topology [42] with a $\beta1(p)\beta3(p)\beta2(a)$ $\beta4(a)\beta5$ arrangement. Helices $\alpha1$, $\alpha2$ and $\alpha4$ are oriented approximately parallel to the direction of the sheet, while helix $\alpha3$ is oriented approximately perpendicular to the direction of the sheet. Helices $\alpha2$ and $\alpha4$ are located on one side of the sheet and display many characteristics of coiled-coil helix interactions as described previously [28]. The active site loop which forms a nob-like protrusion on the exterior of the protein extends from Ala29 at the end of strand

$\beta2$ to Lys36 at the end of the first turn of helix $\alpha2$, encompassing the active site cysteines at positions 32 and 35.

Differences in experimental NMR parameters between the oxidized and reduced states

$^3J_{HN\alpha}$ coupling constants and backbone (NH, ^{15}N, $C^\alpha H$, $^{13}C^\alpha$ and $^{13}C^\beta$) chemical shifts are highly sensitive markers for local conformational and electronic changes. Plots of the differences in $^3J_{HN\alpha}$ coupling constants and chemical shifts between the oxidized and reduced states are provided in Figs 2 and 3, respectively. The accuracy with which the $^3J_{HN\alpha}$ coupling constants are measured is ± 0.5 Hz, so differences greater than 0.8 Hz can be considered significant. Deviations of this magnitude are seen in the middle of helix $\alpha1$ (residue 10), at the beginning (residue 24) and end (residues 28 and 29) of strand $\beta2$, towards the end of helix $\alpha2$ (residue 46), towards the end of strand $\beta3$ (residue
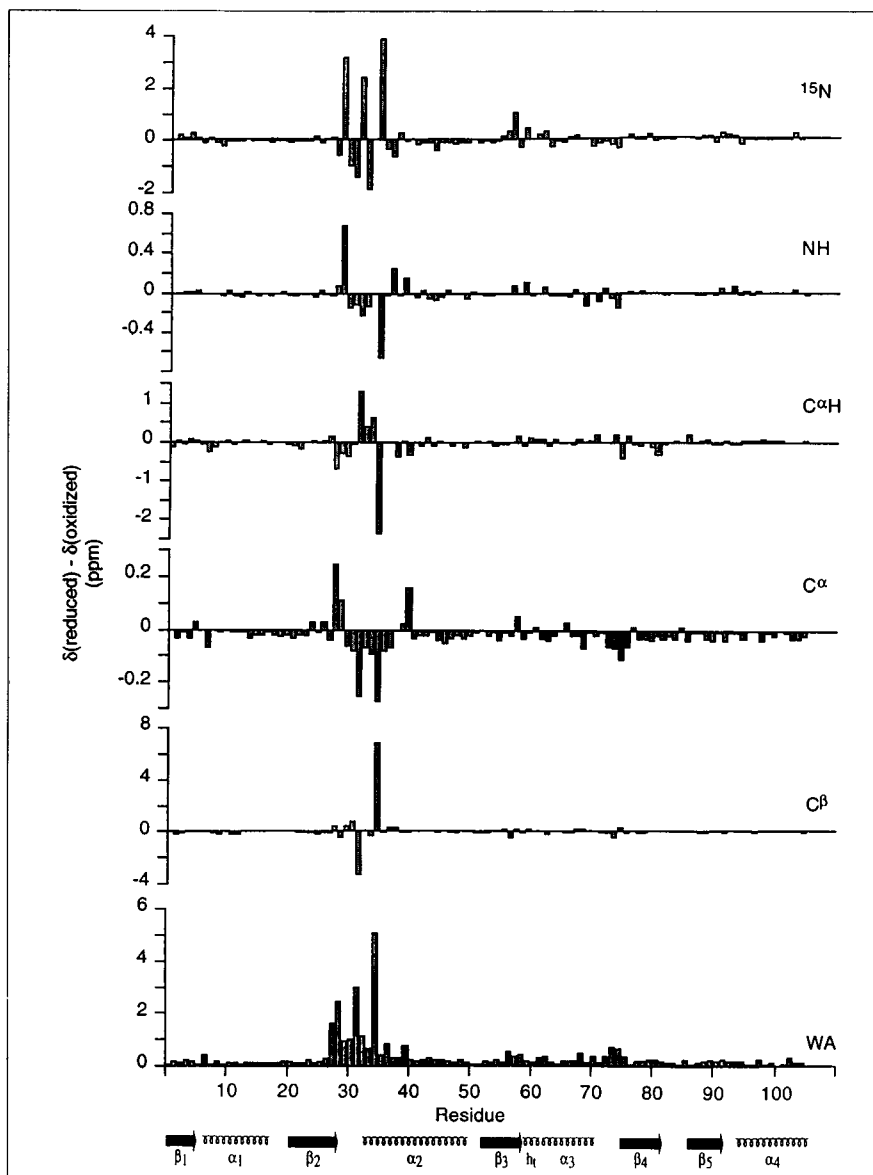
Fig. 3. Difference in backbone (^{15}N, NH, C$^\alpha$H, ^{13}C$^\alpha$ and ^{13}C$^\beta$) chemical shifts between the reduced and oxidized states of the (C62A, C69A, C73A) mutant of human thioredoxin. The bottom graph represents a weighted average, $|WA|$, over the changes of all five atoms, using the formula $|WA| = \Sigma|\delta_{red} - \delta_{ox}|/|\Delta max|$, where the summation extends over the five atoms, and δ_{red} and δ_{ox} are the chemical shifts observed in the reduced and oxidized states, respectively, and Δmax is the largest chemical shift change observed for each type of nucleus [88]. In the case of the chemical shift differences for the two active site cysteine residues at positions 32 and 35, the difference is taken relative to the random coil shifts of free and disulfide linked cysteines (i.e. $\{[\delta_{red} - \delta_{red}(random)] - [\delta_{ox} - \delta_{ox}(random)]\}$ in order to remove the effects of disulfide bond formation on the cysteine chemical shifts.

56), in the small helical turn (residues 58 and 62), at the end of helix α3 (residue 69), and at the beginning of strand β4 (residues 76 and 77). Unfortunately, no accurate values of $^3J_{HN\alpha}$ coupling constants could be measured for the active site (residues 32–35). In contrast to the lack of coupling contant information within the active site, the largest chemical shift differences are observed for a region extending from the end of strand β2 (residue 28) to the middle of helix α2 (residue 40) which includes the active site (residues 29–36). In addition, chemical shift differences are found for residues extending from strand β1 to the beginning of helix α1 (residues 2–9), from the end of strand β3 to the beginning of helix α3 (residues 57–64), and in the loop connecting helix α3 to strand β4 (residues 69–76). Thus, in general, there is good agreement between the coupling constant and chemical shift data.

The principal source of structural information used to compute three-dimensional structures by NMR lies in

the interproton distance information derived from the NOE spectra. There are numerous differences both in pattern and relative intensities spread throughout the structure. Many of these differences, however, are subtle. At a global level, regions that are distinct in the oxidized and reduced structures may be appreciated by a comparison of the number of NOEs observed per residue (Fig. 2e). The largest differences in number of observed NOEs occur in helices α1 and α2. In particular, Leu15 (which is located towards the carboxy-terminal end of helix α1) stands out, exhibiting substantially more NOEs in the oxidized than in the reduced state. Closer inspection of the identity of these NOEs reveals an approximately three-fold increase in medium and long range NOEs. These do not necessarily reflect major structural changes as the r^{-6} dependence of the NOE makes it exquisitely sensitive to the distance separating a given proton pair. Moreover, NOEs can also be attenuated by internal motion. Inspection of the calcu-

Table 1. Structural statistics and atomic rms differences.[a]

	Reduced		Oxidized	
	$<SA_{red}>$	$(\overline{SA_{red}})r$	$<SA_{ox}>$	$(\overline{SA_{ox}})r$
Rms deviations from experimental distance restraints (Å)[b]				
All (2571/2649)	0.008 ± 0.0003		0.006 ± 0.0005	0.010
Inter-residue sequential (|i − j| = 1) (589/521)	0.008 ± 0.0003	0.010	0.003 ± 0.0009	0.004
Inter-residue short range (1 <|i − j|≤ 5) (470/530)	0.009 ± 0.0007	0.015	0.009 ± 0.001	0.014
Inter-residue long range (|i − j| > 5) (677/795)	0.008 ± 0.0006	0.011	0.007 ± 0.0006	0.013
Intra-residue (731/709)[c]	0.005 ± 0.0005	0.005	0.003 ± 0.0003	0.004
Bound water (44/52)[d,e]	0.009 ± 0.002	0.008	0.009 ± 0.002	0.010
Hydrogen bond (60/42)[e]	0.011 ± 0.002	0.008	0.010 ± 0.002	0.010
Rms deviations from complete cross-validated experimental distances (Å)[f]	0.13 ± 0.07		0.13 ± 0.06	
Rms deviations from $^3J_{HN\alpha}$ couping constants (Hz) (89/91)[g]	0.33 ± 0.008	0.36	0.31 ± 0.009	0.32
Rms deviations from experimental dihedral restraints (°) (273/278)[b,h]	0.160 ± 0.015	0.160	0.160 ± 0.024	0.222
Deviations from idealized covalent geometry[i]				
Bonds (Å) (1653/1654)	0.003 ± 0.00005	0.004	0.003 ± 0.00005	0.004
Angles (°) (2985/2986)	0.480 ± 0.003	0.504	0.475 ± 0.005	0.511
Impropers (°) (838/838)	0.227 ± 0.003	0.248	0.225 ± 0.004	0.261
F_{NOE} (kcal mol^{-1})[j]	8.33 ± 0.54	14.1	5.47 ± 0.93	14.5
F_{dihed} (kcal mol^{-1})[j]	0.44 ± 0.09	0.44	0.46 ± 0.15	0.87
F_{coup} (kcal mol^{-1})[j]	10.7 ± 0.5	11.2	8.7 ± 0.5	9.3
F_{repel} (kcal mol^{-1})[j]	13.7 ± 0.6	17.6	13.3 ± 0.9	17.9
E_{L-J} (kcal mol^{-1})[k]	−493 ± 7	−476	−479 ± 7	−472
E_{SFE} (kcal mol^{-1})[k]	−121 ± 3	−126	−122 ± 2	−128
Radius of gyration (Å)	12.91 ± 0.02	12.94	12.89 ± 0.02	12.93

[a]The notation of the NMR structures is as follows: $<SA_{red}>$ and $<SA_{ox}>$ are the ensembles comprising the final 40 simulated annealing structures of the reduced and oxidized states of the (C62A, C69A, C73A) mutant of human thioredoxin, respectively; $\overline{SA_{red}}$ and $\overline{SA_{ox}}$ are the mean structures obtained by averaging the coordinates of the individual structures in the $<SA_{red}>$ and $<SA_{ox}>$ ensembles, respectively, best fitted to each other; $(\overline{SA_{red}})r$ and $(\overline{SA_{ox}})r$ are the restrained minimized mean structures obtained by restrained regularization of the mean structures $\overline{SA_{red}}$ and $\overline{SA_{ox}}$, respectively [74]. The number of terms for the various restraints is given in parentheses and applies to the entire dimer. [b]None of the structures exhibit distance violations greater than 0.3 Å, dihedral angle violations greater than 3°, or $^3J_{HN\alpha}$ coupling constant violations greater than 2 Hz. Furthermore, the average number of $^3J_{HN\alpha}$ coupling constant violations between 1 and 2 Hz is 0.03 ± 0.16 and 1.18 ± 0.74 for the $<SA_{red}>$ and $<SA_{ox}>$ structures, respectively. [c]Only structurally useful intra-residue NOEs are included in the interproton distance restraints. Thus, intra-residue NOEs between protons separated by two bonds or between non-sterospecifically assigned protons separated by three bonds are not incorporated in the restraints. [d]For the reduced protein, the distance restraints involving the six bound water molecules comprise 16 interproton distance restraints between protein protons and water protons and 28 distance restraints relating to hydrogen bonds; for the oxidized protein there are an additional 8 distance restraints for a seventh bound water molecule which comprise 2 interproton distance restraints between protein protons and water protons and 6 distance restraints related to hydrogen bonds. [e]For each backbone hydrogen bond there are two distance restraints: r_{NH-O}, 1.7–2.5 Å; r_{N-O}, 2.3–3.5 Å. These hydrogen bonding restraints account for the slowly-exchanging amide protons and were only included in the final stages of refinement. [f]Simulated annealing with complete cross-validation [41] was carried out on the final set of $<SA_{ox}>$ and $<SA_{red}>$ structures, and the average rms deviation for the test sets comprising ~10 % of the data is reported. (Note that the test set for each structure calculation is different.) [g]The $^3J_{HN\alpha}$ coupling constants included directly in the refinement comprised only those that could be measured from the three-dimensional HNHA experiments to an accuracy of 0.5 Hz or better [52]. Thus, couplings associated with resonances that exhibit overlap of their ^{15}N and NH chemical shifts were not included. [h]The torsion angle restraints comprise 104 φ, 71 ψ, 78 χ₁ and 20 χ₂ angles for the reduced state and 104 φ, 76 ψ, 78 χ₁ and 20 χ₂ angles for the oxidized state. The minimum ranges employed for the φ, ψ, χ₁ and χ₂ restraints were ±10°, ±50°, ±20° and ±20°, respectively. The narrow range for some of the φrestraints was made possible by the availability of highly accurate $^3J_{HN\alpha}$ coupling constant data obtained from the three-dimensional HNHA experiment [52]. In all cases, the angular standard deviations of the torsion angles for the ensemble of $<SA_{red}>$ and $<SA_{ox}>$ structures were much smaller than the ranges employed for the corresponding torsion angle restraints. [i]The improper torsion restraints serve to maintain planarity and chirality. [j]The force constants for the square-well quadratic potentials representing the NOE (F_{NOE}) and dihedral angle (F_{dihed}) restraints and for the harmonic potential representing the coupling constant restraints (F_{coup}) were 50 kcal mol^{-1} Å^{-2}, 200 kcal mol^{-1} rad^{-2} and 1 kcal mol^{-1} Hz^{-2}, respectively. The force constant for the quartic van der Waals repulsion term (F_{repel}) is 4 kcal mol^{-1} Å^{-4} with the hard sphere van der Waals radii set to 0.8 times their values in the CHARMM PARAM19/PARAM20 energy parameters [83,84]. $^kE_{L-J}$ is the Lennard–Jones van der Waals energy calculated with the CHARMM [83,84] empirical energy function and E_{SFE} is the solvation free energy of folding calculated as described in [85]. These two terms are not included in the target function for simulated annealing or restrained minimization.

lated structures does indeed reveal that Leu15 is more closely packed in the oxidized than in the reduced state against residues located in the carboxy-terminal end of strand β4, the loop connecting β4 and β5, and the amino-terminal end of strand β5 (residues 8–85). Table 3 summarizes some of the major differences in long range NOE contacts between the reduced and oxidized states as defined by the presence of NOEs between a particular residue pair in one state and their absence in another state. The majority of these involve NOE side chain–side chain contacts across the strands and between strands and helices within the protein core, indicative of minor side chain rearrangements. In addition, there are significant differences in the NOEs in-

Table 2. Atomic rms differences and torsion angle deviations for the simulated annealing structures of the reduced and oxidized states of the (C62A, C69A, C73A) mutant of human thioredoxin.

Atomic rms differences (Å)	Backbone atoms	All atoms	All ordered atoms[b]
Reduced			
$<SA_{red}>$ vs $\overline{SA}_{red}$	0.19 ± 0.02	0.60 ± 0.03	0.30 ± 0.02
$<SA_{red}>$ vs $(\overline{SA}_{red})r$	0.20 ± 0.02	0.69 ± 0.04	0.35 ± 0.03
$(\overline{SA}_{red})r$ vs $\overline{SA}_{red}$	0.08	0.34	0.17
Oxidized			
$<SA_{ox}>$ vs $\overline{SA}_{ox}$	0.18 ± 0.02	0.58 ± 0.03	0.31 ± 0.03
$<SA_{ox}>$ vs $(\overline{SA}_{ox})r$	0.20 ± 0.02	0.65 ± 0.05	0.36 ± 0.04
$(\overline{SA}_{ox})r$ vs $\overline{SA}_{ox}$	0.08	0.34	0.17
Reduced *versus* oxidized			
$<SA_{red}>$ vs $<SA_{ox}>$	0.92 ± 0.04	1.31 ± 0.05	1.07 ± 0.05
$\overline{SA}_{red}$ vs $\overline{SA}_{ox}$	0.86	1.00	0.94
$(\overline{SA}_{red})r$ vs $(\overline{SA}_{ox})r$	0.85	1.07	0.96
$<SA_{red}>$ vs $\overline{SA}_{ox}$	0.88 ± 0.04	1.16 ± 0.05	0.99 ± 0.04
$<SA_{ox}>$ vs $\overline{SA}_{red}$	0.88 ± 0.04	1.15 ± 0.04	0.99 ± 0.04

Angular standard deviations (°)[c]	$<SA_{red}>$	$<SA_{ox}>$
ϕ	1.4 ± 2.6 (104)	1.4 ± 2.2 (104)
ψ	2.9 ± 3.4 (104)	3.3 ± 3.6 (104)
χ_1	8.2 ± 16.7 (89)	8.4 ± 16.2 (89)
$\chi_1{}^d$	2.7 ± 2.2 (80)	3.5 ± 4.1 (81)
χ_2	29.8 ± 29.8 (64)	28.7 ± 29.4 (64)
$\chi_2{}^d$	6.5 ± 8.5 (38)	7.0 ± 9.6 (38)

[a]The notation of the structures is the same as in Table 1. [b]The atoms included comprise all N, C^α, C, O and C^β atoms of residues 1–105; all water molecules; the complete side chains of residues 2, 5, 7–9, 10, 11, 14, 15, 17–19, 22–25, 27, 29–35, 38, 40–43, 45, 46, 49–55, 57, 59, 60, 62, 65–67, 69, 71, 73–80, 83, 86–92, 97 and 99–105; and the side chains of Met1 up to C^β, Lys3 up to C^γ, Gln4 up to C^δ, Glu6 up to C^γ, Lys8 up to C^δ, Gln8 up to C^δ, Gln12 up to C^β, Glu13 up to C^γ, Asp16 up to C^γ, Asp20 up to C^γ, Lys21 up to C^δ, Asp26 up to C^γ, Ser28 up to C^β, Lys36 up to C^δ, Met47 up to C^β, Lys39 up to C^δ, Ser44 up to C^β, Glu47 up to C^γ, Lys48 up to C^δ, Glu56 up to C^δ, Asp58 up to C^γ, Asp61 up to C^γ, Gln63 up to C^β, Asp64 up to C^γ, Glu68 up to C^ϵ, Glu70 up to C^δ, Lys72 up to C^γ, Lys81 up to C^δ, Gln84 up to C^γ, Lys85 up to C^δ, Glu88 up to C^β, Asn93 up to C^γ, Lys94 up to C^γ, Glu95 up to C^γ, Lys96 up to C^δ, and Glu98 up to C^γ. [c]The number of residues is given in parentheses. [d]Angular standard deviations for χ_1 and χ_2 angles, excluding angles with angular deviations of ≥ 40°.

volving the active site residues, Ala29 and Trp31, specifically to Asp60 in the helical turn and to Pro75 in strand β4 which are present in the reduced state but not the oxidized state. Interestingly, a large number of the residues in Table 3 are conserved in all thioredoxins and have been proposed to reside in the interaction sites with other proteins [3].

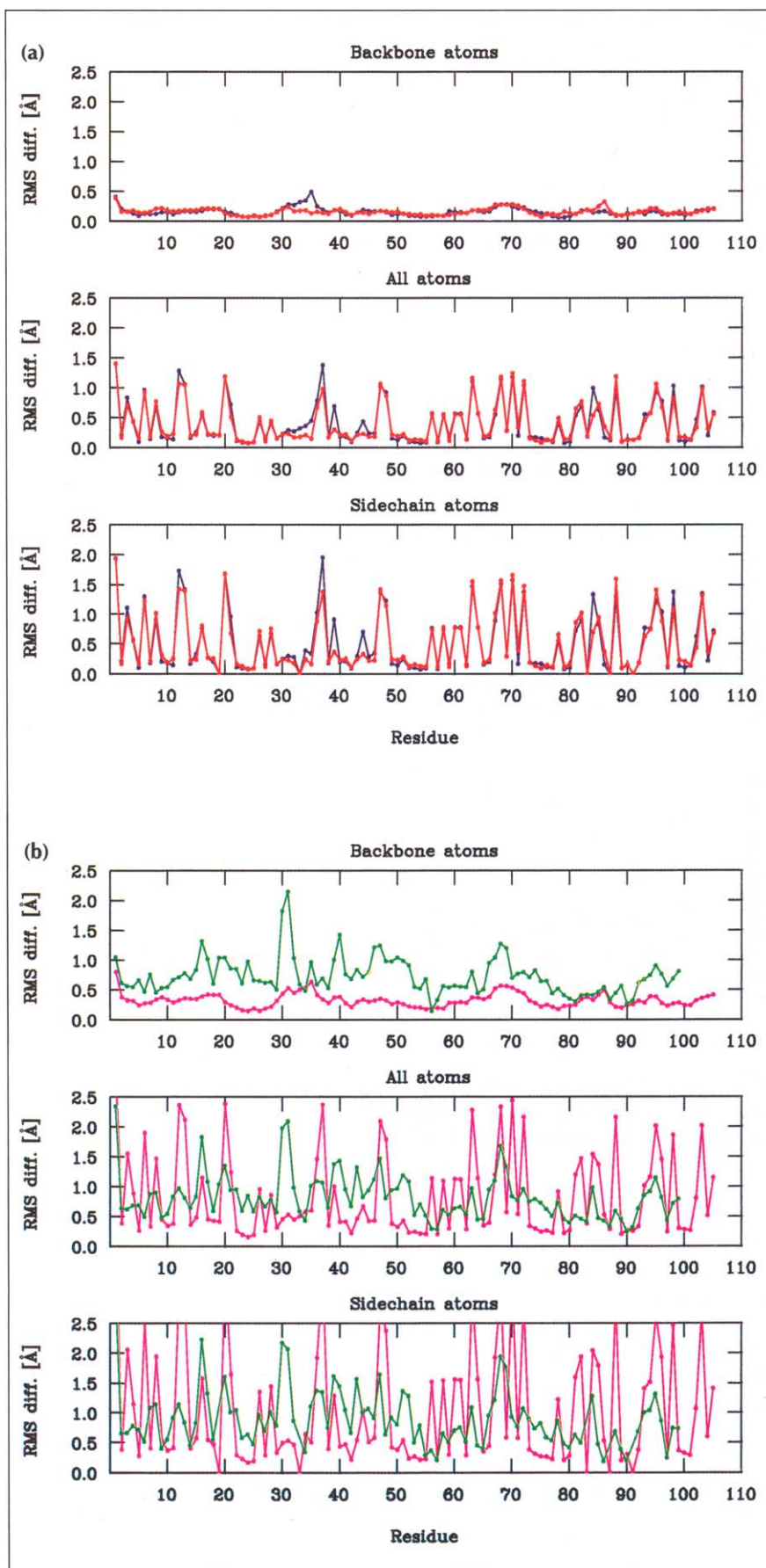## Structural differences between the oxidized and reduced states

A superposition of the backbone atoms for the ensemble of simulated annealing structures of the reduced and oxidized states (40 structures each) is shown in Fig. 6c, and a superposition of the backbone of the mean coordinates is shown in Fig. 7. From these figures it is apparent that although the overall difference between the two states is small, regions of noticeable differences exist, as manifested by areas where the ensem-

ble of structures for the two states do not overlap (Fig. 6c). A quantitative assessment of whether the regions of difference are significant can be obtained by comparing the atomic rms differences between the mean coordinate positions with the sum of the coordinate precisions for the two ensembles (Fig. 4b). The overall ratio for these two numbers is ~2.3 for the backbone atoms, ~0.9 for all atoms and ~1.5 for all ordered atoms. Whenever this ratio exceeds one, the probability of the two ensembles being genuinely different is greater than 95%. Significant differences at the local level can be extracted by comparing the torsion angle rms differences between the two mean coordinates with the sum of the torsion angle standard deviations for the two ensembles (Fig. 5b). In general, the areas of difference at the structural level correlate well with the chemical shift and coupling constant differences discussed above.

Inspection of the data in Figs 4b, 5b, 6c and 7 reveal that the most significant backbone differences are found in the active site, in particular residues 30–32, in helices $\alpha2$, $\alpha3$ and $\alpha4$, and in the loop connecting helix $\alpha1$ and strand $\beta2$.

A detailed view of the active site, including side chains, is provided by the superposition of the restrained minimized mean structures of the oxidized and reduced states shown in Fig. 8a. Substantial differences (> 15°) in the ϕ torsion angles of residues Ser28, Ala29, Thr30, Trp 31, Cys32, Cys35 and Lys36 and in the ψ angles of residues Ser28, Ala29, Thr30, Pro34, Cys35 and Lys36 are observed between the reduced and oxidized states. This can be attributed to a slight shortening of the C^α–C^α distance by approximately 0.1 Å between Cys32 and Cys35 upon formation of the disulfide bond (Table 4), and a change in the χ_1 angle of Cys35 from −50.9 ± 3.1° in the reduced state to −39.1 ± 0.7° in the oxidized state. The latter difference is clearly apparent in Fig. 8a. The difference in the χ_1 angle of Cys32 in the two states (166.5 ± 1.1° in the reduced form and 160.6 ± 0.8° in the oxidized form), on the other hand, is much smaller. Associated with this, the parameters for the hydrogen bond between the S^γ atom of Cys32 and the backbone amide of Cys35, which is in part responsible for the anomalously low pK_a (~6.3) of Cys32 [43] and hence its high reactivity [11], are very similar in the two oxidation states (Table 4). Indeed, the S^γ (Cys32)–NH(Cys35) and S^γ (Cys32)–N(Cys35) distances in the two states are identical within the errors of the current coordinates, and the only significant change is a ~9° reduction in the S^γ (Cys32)–NH(Cys35)–N(Cys35) angle upon oxidation. This suggests that the hydrogen bond between S^γ (Cys35) and NH(Cys35) is slightly weaker in the oxidized than in the reduced state. Thus, the ~1.1 Å reduction in the S^γ–S^γ distance from 3.11 ± 0.08 Å in the reduced state to 2.02 ± 0.01 Å in the oxidized state is mainly accomplished by a change in the χ_1 angle of Cys35, as well as accommodating backbone changes.

Fig. 4. (a) Atomic root mean square (rms) distribution of the individual simulated annealing structures about the mean coordinate positions for reduced (blue) and oxidized (red) states of the (C62A, C69A, C73A) mutant of human thioredoxin. **(b)** Comparison of the atomic rms difference between the restrained minimized mean structures of the reduced and oxidized states of the (C62A, C69A, C73A) mutant of human thioredoxin (green) with the sum of the atomic rms distribution about the mean coordinate positions for the oxidized and reduced states (magenta).
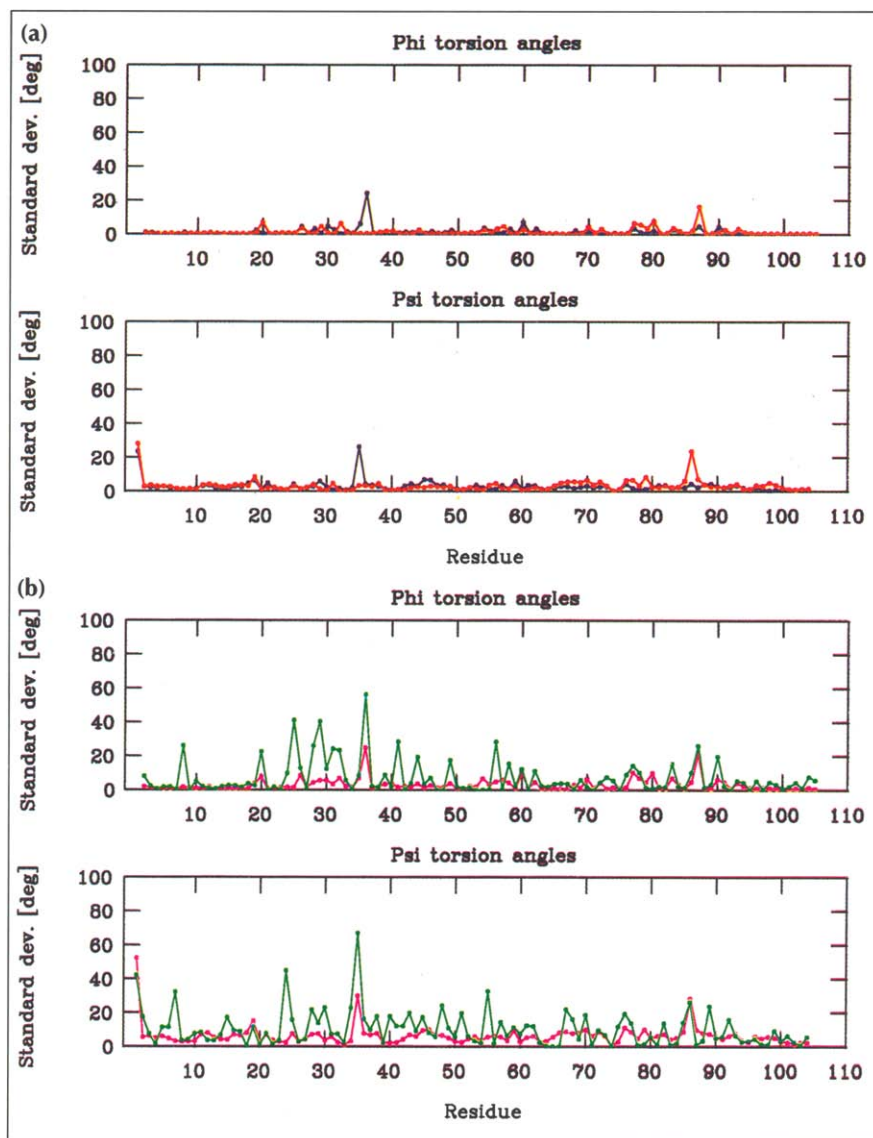
Fig. 5. (a) Angular standard deviations for the backbone torsion angles for the simulated annealing structures of the reduced (blue) and oxidized (red) states of the (C62A, C69A, C73A) mutant of human thioredoxin as a function of residue number. **(b)** Comparison of the angular rms difference between the restrained minimized mean structures of the reduced and oxidized states of the (C62A, C69A, C73A) mutant of human thioredoxin (green) with the sum of the angular standard deviations for the oxidized and reduced states (magenta).

The small difference in the position of the Trp31 side chain in the two states is also easily appreciated from Fig. 8a and is mainly attributable to the changes in backbone torsion angles and a 10° change in the χ_2 angle (from $-77.8 \pm 2.0°$ in the reduced state to $-87.0 \pm 2.1°$ in the oxidized state). The χ_1 angle of Trp31, on the other hand, is only minimally altered ($54.8 \pm 1.3°$ and $59.1 \pm 1.4°$ in the reduced and oxidized states, respectively). These minor changes in the environment of Trp31 are borne out spectroscopically since only marginal differences are observed in the tryptophan fluorescence spectrum between the reduced and oxidized (C62A, C69A, C73A) mutant of human thioredoxin (unpublished data).

The differences in the helices between the two states arise from rigid-body motions of the helices relative to the underlying sheet. This can be appreciated qualitatively from the superpositions shown in Figs 6c and 7, and quantitatively by the C^α–C^α distances from the

terminal residues in the helices to residues in the underlying sheet (Table 5). Helices α2 and α3 are displaced outwards at their carboxyl termini in the oxidized state relative to the reduced state. Thus, the C^α–C^α distances at the amino termini of helices α2 and α3 between Cys35(α2) and Ser28(β2) and between Ala62(α3) and Glu6(β1), respectively, are the same in the oxidized and reduced states. The C^α–C^α distances at the carboxyl termini of helices α2 and α3, on the other hand, between Ser46(α2) and Phe54(β3) and between Ala69(α3) and Lys85(β5) are 18% and 13% longer, respectively, in the oxidized state relative to the reduced state. The orientation of helix α4 with regard to the underlying sheet remains essentially unchanged (Table 5), but it appears to exhibit a systematic sliding displacement between the two states (Fig. 7a). Finally, the orientation of helix α1 with regard to the underlying sheet also remains unchanged but it is packed slightly more tightly against residues 80–85 comprising the end of strand β4 and the beginning of strand β5. This is
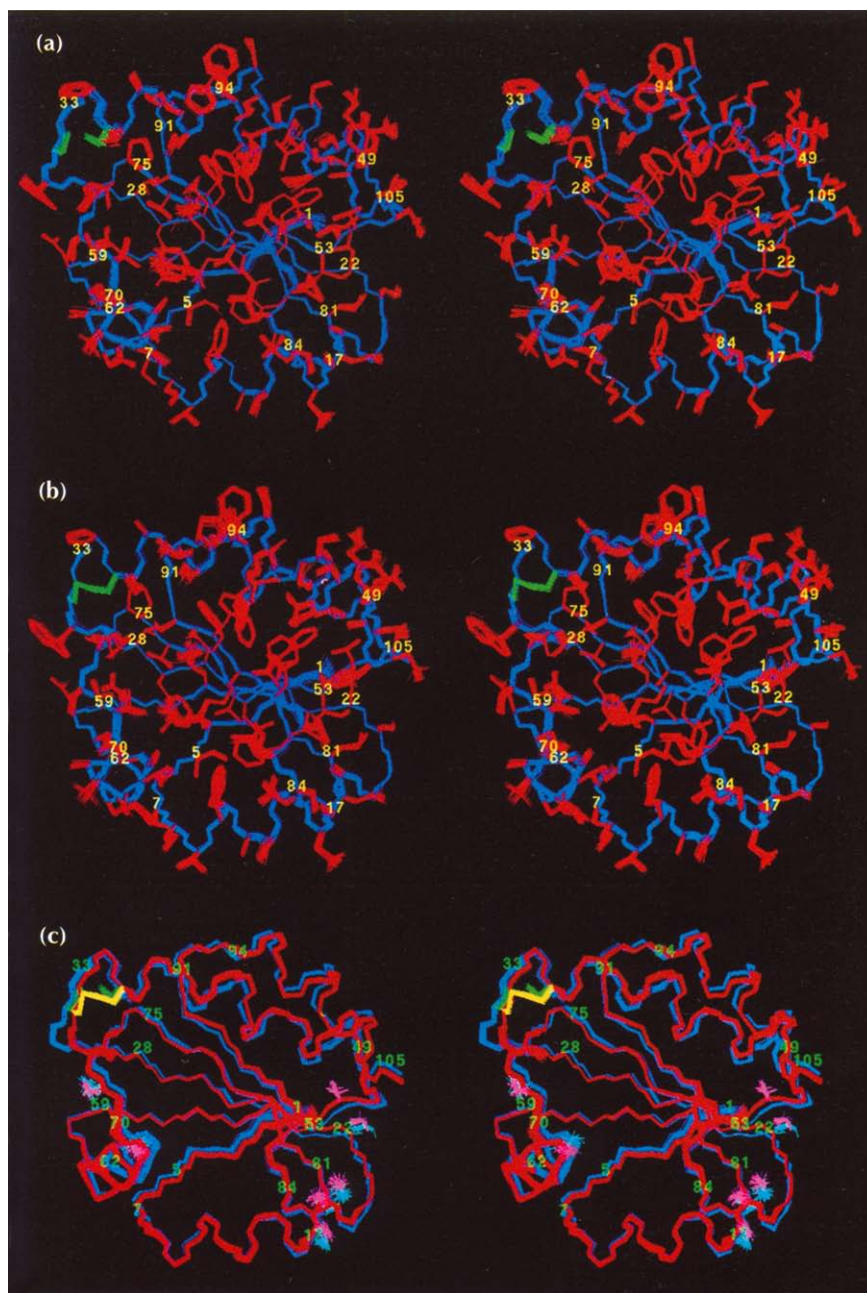
Fig. 6. Superpositions of the 40 final simulated annealing structures of the reduced and oxidized states of the (C62A, C69A, C73A) mutant human thioredoxin. Stereoviews of the best fit superposition of the backbone, ordered side chains and active site cysteines for the reduced **(a)** and oxidized **(b)** states, respectively. The backbone atoms, the side chains and active site cysteine residues are shown in blue, red and green, respectively. **(c)** Stereoview showing a best fit superposition of the backbone (N, C$^{\alpha}$, C) atoms, the active site cysteine residues and the bound water molecules of the oxidized and reduced states. The backbone, active site cysteine residues and bound water molecules (V-shaped) are shown in blue, green and blue, respectively, for the reduced state, and in red, yellow and pink for the oxidized state, respectively. The models were generated with the program AVSXPLOR [86].

reflected by a 5 % reduction in the C$^{\alpha}$–C$^{\alpha}$ distance between Leu15(α1) and Phe80(β4) in the oxidized relative to the reduced state (Table 5).

As viewed in Fig. 7b, there is also a difference in the apperture of the central cleft formed by the active site and the two opposing loops (residues 74–76 and 90–92) which is associated with the changes in the orientation of helices α2 and α4. This is reflected in a ~10 % increase in the C$^{\alpha}$–C$^{\alpha}$ distances between the triad formed by Cys35, Pro72 and Ala92 upon oxidation (Table 5). Thus, the packing of the surface side chains in this region of the protein is slightly tighter in the reduced state than in the oxidized state. Interestingly, this is the site of proposed protein–protein contacts between thioredoxin and other proteins [2,3,19].

The packing of side chains within the protein core is very similar between the two states and is illustrated in Fig. 8b. Indeed, there are only 17 and 7 residues that exhibit a difference in χ_1 and χ_2 angles, respectively, of greater than 10° between the two states that can be considered significant (i.e. where the sum of the torsion angle rms deviations of the two ensembles of structures is less than the angular rms difference between the mean coordinates of the two states). These residues comprise Gln4, Lys21 and Ile38 for χ_1 and χ_2, Ser7, Lys8, Thr30, Cys35, Phe42, Ser46, Ser50, Asn51, Asp64, Val71, Gln84, Ser90, Glu95 and Val105 for χ_1 only, and Ile5, Phe27, Trp31 and Gln78 for χ_2 only. Only 8 of these 21 residues are completely buried with surface accessibilities of <15 Å^2, namely Ile5, Phe27, Cys35, Ile35, Ile38, Phe42, Ser46, Val71 and Gln78.

Table 3. Major differences in long range NOE contacts between the reduced and oxidized states of the (C62A, C69A, C73A) mutant of human thioredoxin.[a]

NOE contact		Reduced	Oxidized
Lys3 (β1)	Glu56 (β3)	+	−
Ile5 (β1)	Asp58 (β3)	−	+
Phe11* (α1)	Phe80 (β4)	+	−
Val24* (β2)	Ile53 (β3)	+	−
Asp26* (β2)	Leu55 (β3)	+	−
Asp26* (β2)	Gln78 (β4)	−	+
Phe27* (β2)	Glu56 (β3)	+	−
Ser28 (β2)	Thr76 (β4)	−	+
Ala29* (AS)	Asp60* (HT)	+	−
Ala29* (AS)	Pro75* (β4)	+	−
Trp31* (AS)	Asp60* (β3)	+	−
Thr76 (β4)	Gly91* (β5)	−	+
Phe77 (β4)	Gly91* (β5)	−	+
Phe77 (β4)	Asn93	+	−
Phe77 (β4)	Lys94 (α4)	+	−
Gln78 (β4)	Glu89 (β5)	+	−

[a]Only contacts that are present in one oxidation state (indicated by a plus sign) but absent in the other (indicated by a minus sign) are summarized. The asterisks indicate residues that are conserved in all species of thioredoxins. The location of the residue within particular secondary structure elements is indicated in parentheses (AS indicates the active site, and HT signifies a helical turn; Asn93 is located just prior to the start of helix α4 at residue 94).

Table 4. Comparison of the active site conformation involving the cysteine residues in the oxidized and reduced states of the (C62A, C69A, C73A) mutant of human thioredoxin.[a]

|	$<SA_{red}>$	$<SA_{ox}>$	E. coli oxidized[a]
Distance (Å)			
Cys32 C^α–Cys35 C^α	5.65 ± 0.05	5.54 ± 0.02	5.22/5.16
Cys32 S^γ–Cys35 S^γ	3.11 ± 0.08	2.02 ± 0.01	2.09/2.05
Cys32 S^γ–Cys35 N	3.12 ± 0.03	3.08 ± 0.01	3.23/3.20
Cys32 S^γ–Cys35 NH	2.22 ± 0.03	2.25 ± 0.01	−
Angle (°)			
C32$^\gamma$–C35NH–C35N	151.6 ± 2.2	142.5 ± 0.7	
Disulfide bond torsion angles (°)			
χ_2 (C32)	166.5 ± 1.1	160.6 ± 0.8	165/167
χ_2	−165.1 ± 1.6[b]	−160.5 ± 1.0	−132/−136
χ_3	61.8 ± 4.7[b]	72.6 ± 0.5	81/72
χ_2'	89.7 ± 1.1[b]	85.7 ± 0.4	79/82
χ_1' (C35)	−50.9 ± 3.1	−39.2 ± 0.7	−62/−62

[a]Values are given for molecules 1 and 2 in the asymmetric unit (from [26]).
[b]The values are given for the χ_2, χ_3 and χ_2' torsion angles for the reduced state of human thioredoxin across a virtual S^γ(Cys32)–S^γ(Cys35) bond.

Another method of assessing differences in side chain conformations and packing is to examine the differences in surface accessibility. The surface accessibility of only five residues is increased by more than 12.5 Å^2 in the oxidized state relative to the reduced
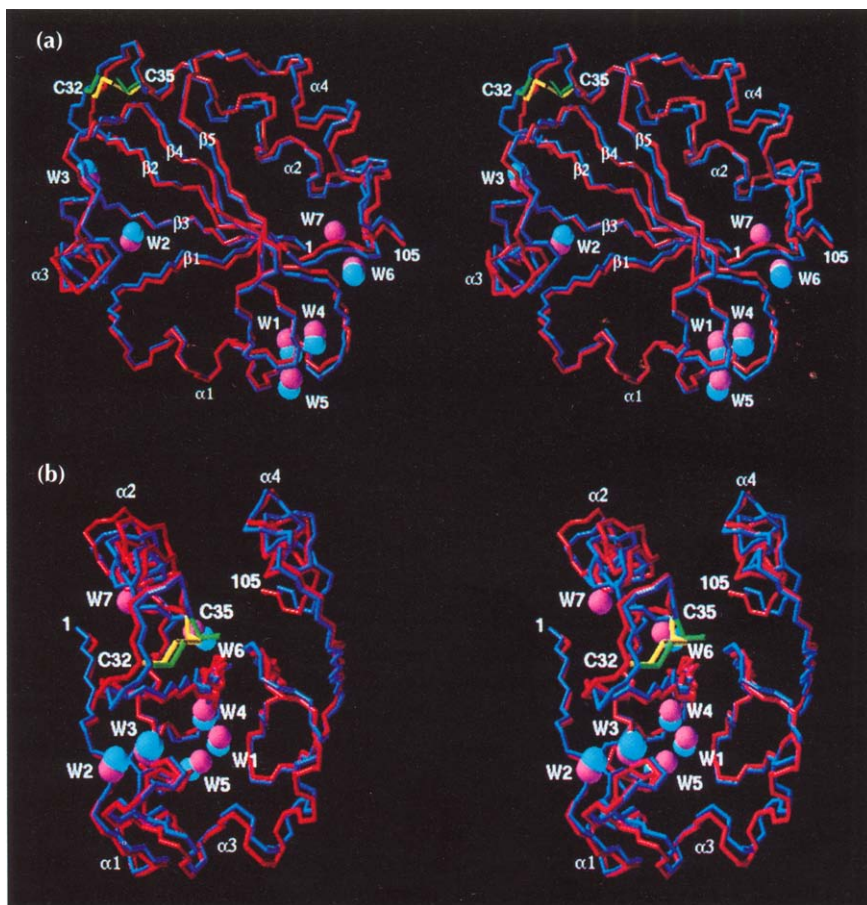
Fig. 7. Two stereoviews (a),(b) showing a best fit superposition of the backbone (N, C^α, C) atoms of the restrained minimized mean structures of the reduced and oxidized states of the (C62A, C69A, C73A) mutant of human thioredoxin. The backbone atoms, cysteine side chains and bound water molecules (spheres) are shown in blue, green and blue, respectively, for the reduced form, and in red, yellow and pink, respectively, for the oxidized form. Note the presence of an additional bound water, W7, in the oxidized form. The models were generated with the program VISP [87].
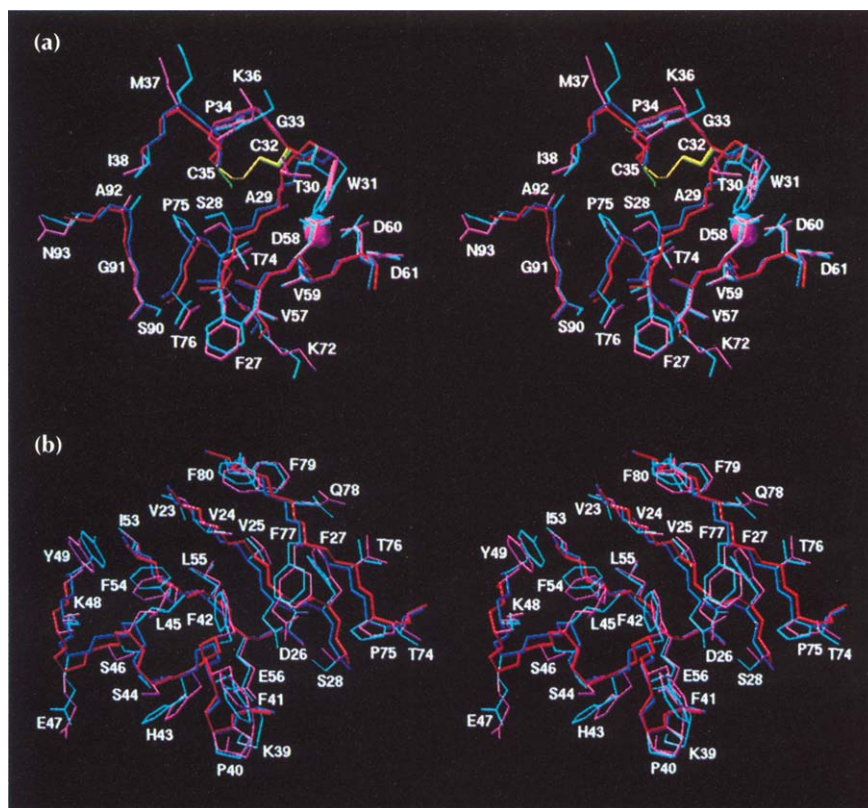
Fig. 8. Best fit superposition of (a) the active site and (b) a portion of the hydrophobic core of the restrained minimized mean structures of the reduced and oxidized states of the (C62A, C69A, C73A) mutant of human thioredoxin. The backbone and side chains are shown in dark and light blue, respectively for the reduced form, and in red and pink, respectively, for the oxidized form. The models were generated with the program VISP [87].

state, namely Ser46, Glu47, Glu70, Thr74 and Thr75, and only one of these (Glu47) is increased by more than $25 Å^2$. In a similar vein, the surface accessibility of only five residues is increased by more than $12.5 Å^2$ in the reduced state relative to the oxidized state, namely Met1, Gln4, Thr30, Ile53 and Lys81, and none is increased more than $25 Å^2$. Further, the differences in surface accessibility for Met1 and Glu70 cannot be considered significant as they are smaller than the sum of the rms deviations in their respective surface accessibilities for the ensemble of reduced and oxidized structures.

Differences in water structure in the reduced and oxidized states

Using 2D H_2O-NOE/rotating frame Overhauser enhancement (ROE)-^1H–^{13}C heteronuclear single quantum correlation (HSQC) and H_2O-ROE-^1H–^{15}N HSQC spectroscopy [44–46], we were able to ascertain the location of six bound water molecules in the reduced state plus an additional bound water in the oxidized state. Examples of these spectra are shown in Fig. 9, and the location of the bound waters is displayed in Figs 6c, 7 and 10. Three of these water molecules were previously identified in the reduced wild-type structure [47]. Waters W1, W4 and W5 are involved in bridging backbone hydrogen bonds between the turn connecting helix α1 and strand β2 and the turn connecting strands β4 and β5. They form a triangular hydrogen-bonded cluster of water molecules. Water W1 accepts hydrogen bonds from the backbone amides of Lys83

and Gly83 and donates a hydrogen bond to the backbone carbonyl of Gly19. The amide proton of Gly19 is in turn hydrogen bonded to water W5 which also donates a hydrogen bond to Leu15. The third water molecule of this triad, W4, bridges the backbone carbonyl of Ala18 with the backbone amide proton of Lys21. Water W2 bridges backbone hydrogen bonds between the end of strand β1 (backbone carbonyl of Ile5) and the helical turn between strands β3 and helix α3 (backbone amide of Asp58). Water W3 is involved in bifurcating hydrogen bonds stabilizing the helical turn between strands β3 and helix α3. It is located in a pocket lined on two sides by the side chains of Ala29 and Val59, and accepts a hydrogen bond from the backbone amide of Asp60 and donates hydrogen bonds to the side chain carboxyl groups of Asp60 and Asp58. Asp60 and Asp58 are also hydrogen bonded to the side chain $N^{ε1}H$ of Trp31 and the backbone amide of Thr30, respectively. Water W6 is involved in bridging hydrogen bonds between the backbone amide of the amino-terminal residue of strand β2 (Leu22) and the backbone carbonyl of Asn51 in the turn connecting helix α3 and strand β3. Finally, water W7, which is only observed in the oxidized state, is involved in bridging hydrogen bonds that stabilize the turn between helix α2 and strand β3, accepting a hydrogen bond from the backbone amide of Val52 and donating hydrogen bonds to the backbone carbonyls of Tyr49 and Val52. In the case of W1, W3, W4 and W5, negative NOEs are observed indicating a residency time greater than

Table 5. Comparison of some conformationally sensitive distances in the oxidized and reduced states of the (C62A, C69A, C73A) mutant of human thioredoxin.[a]

	C^α–C^α distance (Å)	
	$<SA_{red}>$	$<SA_{ox}>$
Helix–sheet orientations		
Helix α1		
11(α1)–5(β1)	6.22 ± 0.08	5.92 ± 0.06
15(α1)–23(β23)	7.54 ± 0.09	7.58 ± 0.08
15(α1)–80(β4)	8.30 ± 0.12	7.94 ± 0.08
18(α1)–53(β3)	6.85 ± 0.08	6.99 ± 0.22
Helix α2		
35(α2)–28(β2)	5.95 ± 0.14	6.24 ± 0.06
39(α2)–56(β3)	9.11 ± 0.15	9.81 ± 0.20
46(α2)–54(β3)	6.34 ± 0.10	7.45 ± 0.14
Helix α3		
62(α3)–6(β1)	5.12 ± 0.07	5.24 ± 0.06
69(α3)–85(β5)	9.87 ± 0.10	11.14 ± 0.28
Helix 4		
96(α4)–91(β5)	8.82 ± 0.08	8.99 ± 0.08
104(α4)–86(β5)	8.22 ± 0.10	8.29 ± 0.20
Triad between catalytic site and loops		
preceding strand β4 and helix α4		
Cys35–Pro75	5.90 ± 0.20	6.42 ± 0.08
Cys35–Ala92	7.87 ± 0.15	8.46 ± 0.12
Pro75–Ala92	6.10 ± 0.08	6.64 ± 0.13

[a]The notation of the structures is the same as that given in footnote a to Table 1.

about 500 ps; the NOEs for waters W2, W6 and W7, on the other hand, are too weak to be observed and only ROEs are seen, indicating a residency time between 200–500 ps [46,48].

In addition to waters whose positions can be clearly defined with regard to hydrogen bond donors and acceptors, further interactions with water are observed at the surface of the protein. Indeed, almost all surface exposed methyl groups give rise to ROEs with water. For the majority of these no NOEs could be detected indicating lifetimes in the 200–500 ps range. A small number, however, namely Ala17, Val86, Leu104 and Val105, exhibited positive NOEs indicative of lifetimes < 300 ps. It is also interesting to note that some aspects of surface water are clearly different between the two oxidiation states. Thus, in addition to NOEs involving water W7, negative NOEs to water are observed for the methyl groups of Leu15, Val25, and Leu55 in the oxidized but not the reduced state. These form a cluster of hydrophobic residues at the surface of the protein (Fig. 10). Similarly, the ROE from water to the $C^\gamma H_3$ methyl group of Ile5 is only observed in the reduced state, but no NOE is observed for this interaction indicating a lifetime of 200–500 ps. Interestingly, changes in the solvent layer around the protein surface have been invoked to explain the difference in adiabatic compressibility observed for reduced and oxidized E. coli thioredoxin [17]. It remains to be established whether the differ-

ences observed in bound water structure for human thioredoxin are in any way connected with the large difference in partial specific volume for the E. coli protein.

Functional implications of the structures of reduced and oxidized human thioredoxin

What are the crucial differences between the oxidized and reduced states of human thioredoxin and how may they further our understanding of its enzymatic function and shed light on its numerous non-redox related functions? The present structures reveal that the differences between the two states are indeed very small and subtle. To detect these minor differences with confidence it was essential to determine highly-refined structures for both states. Such data were not previously available. A superposition of the active site regions for oxidized E. coli thioredoxin (both molecules within the asymmetric unit) and reduced and oxidized human thioredoxin is depicted in Fig. 11. All four structures are very similar in this region, both with respect to the backbone conformation and side chain orientations. The location of the Trp31 side chain is essentially identical in the reduced and oxidized structures, being held in place by a hydrogen bond between the $N^{\epsilon 1}H$ proton and the side chain carboxyl group of Asp60. The presence of this hydrogen bond is indicated by the downfield shifted resonances for both the $N^{\epsilon 1}H$ and $^{15}N^{\epsilon 1}$ resonances of Trp31. In addition, both resonances titrate with a pK_a of ~3.8, characteristic of an aspartate side chain. This side chain–side chain interaction connects the helical turn between strand β3 and helix α3 to the active site region, namely the loop between strand β2 and helix α2, thereby closing off part of the interior of the protein and determining the relative orientation of these two loops. The orientation of the side chain of Trp31 in the human thioredoxin structures is slightly different from that observed in the E. coli structures due to small changes in backbone torsion angles throughout the active site region as well as small differences in χ_1 and χ_2 angles. These differences are probably the result of crystal packing in the X-ray structure.

Given the close similarity between the active sites of the human and E. coli proteins, it is possible that the difference in activity between the reduced and oxidized states with regard to non-redox functions may not only be related to the small structural differences between the isolated reduced and oxidized states, but also to their ability to undergo the appropriate conformational changes when interacting with target proteins. The formation of the disulfide bond makes the active site and the two opposing loops (residues 74–76 and 90–92) that constitute all known interacting sites on thioredoxin [2,3,19]), more rigid [20]. Hence, the conformational entropy of the oxidized state is diminished relative to that of the reduced state, and it is therefore possible that the oxidized state of thioredoxin cannot adopt the appropriate conformation, thereby rendering it inactive.
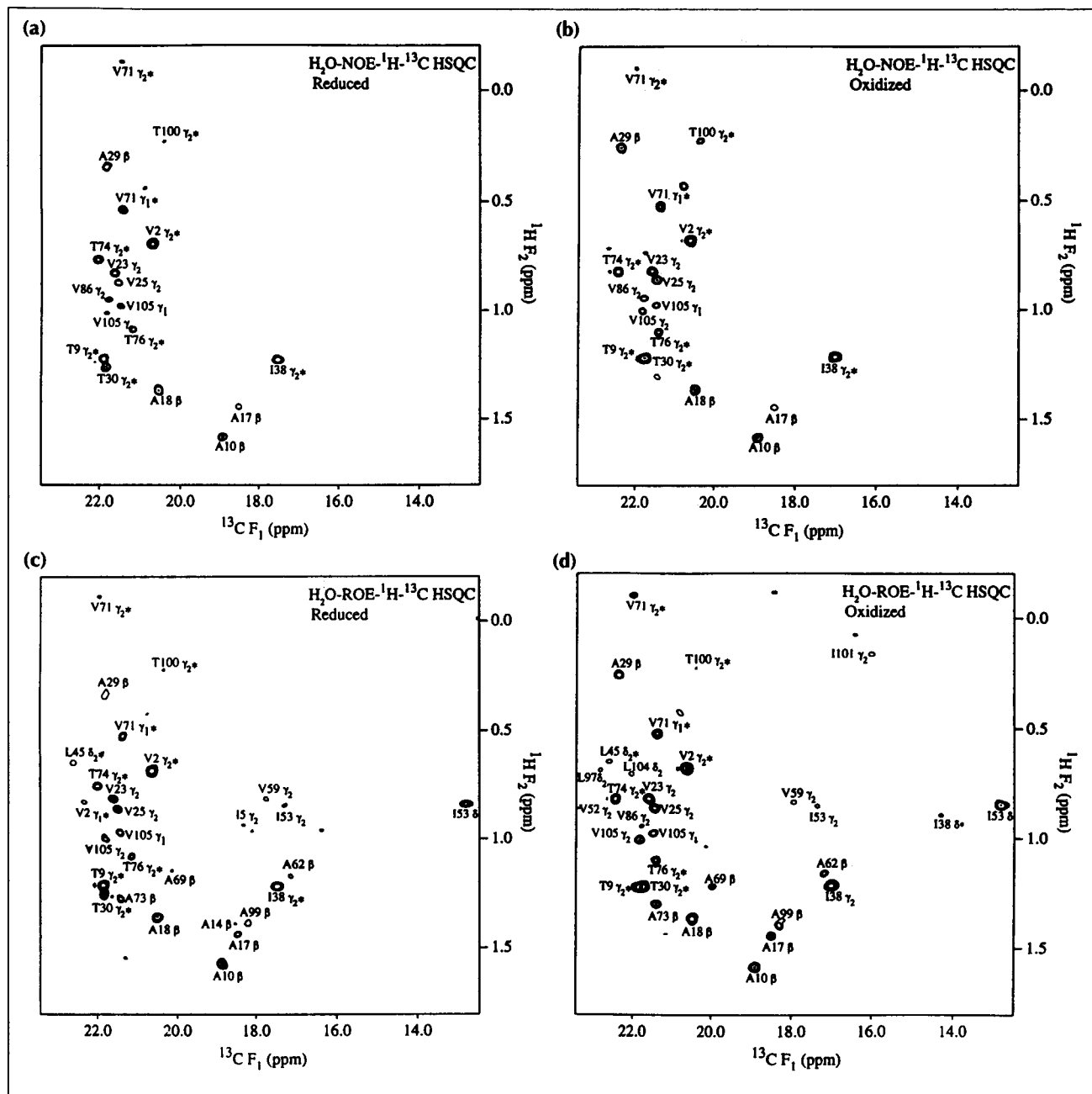
Fig. 9. The methyl region of the H_2O-NOE-^1H-^{13}C HSQC spectrum for **(a)** the reduced and **(b)** the oxidized state of the (C62A, C69A, C73A) mutant of human thioredoxin. The methyl region of the H_2O-ROE-^1H-^{13}C HSQC spectrum for **(c)** the reduced and **(d)** the oxidized state of the (C62A, C69A, C73A) mutant of human thioredoxin. All spectra were recorded with NOE and ROE mixing times of 100 ms and 60 ms, respectively.

Biological implications

Thioredoxin is a ubiquitous protein found throughout all living organisms. The active site of the enzyme contains two redox active cysteines within the conserved sequence Trp-Cys-Gly-Pro-Cys (residues 31 to 35). The dithiol form of the protein is a powerful general protein disulfide reductase and the disulfide-containing oxidized form can be reduced to the dithiol form again by reduced nicotinamide adenine dinucleotide phosphate and thioredoxin reductase. Thioredoxin is involved in a variety of fundamental biological functions; it acts as a hydrogen donor for ribonucleotide reductase, regulates the activity of photosynthetic enzymes, and is involved in the induction of interleukin-2 receptor expression and the activation of the transcription factor NF-κB. In addition to the above processes which involve thioredoxin as an oxidoreductase, others, like its
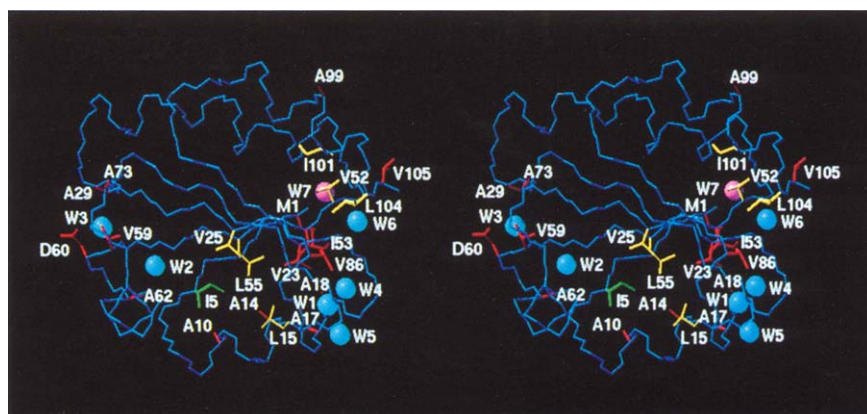
Fig. 10. Location of bound waters in the (C62A, C69A, C73A) mutant of human thioredoxin. The backbone (of the oxidized state) is shown in blue, the tightly bound waters that are common to the reduced and oxidized states as blue spheres, and the additional tightly bound water in the oxidized form in pink. Surface side chains that exhibit ROEs to water in both the oxidized and reduced states are shown in red, surface side chains that exhibit ROEs to water in the reduced state but not the oxidized state in green, and surface side chains that exhibit ROEs to water in the oxidized state but not the reduced state in yellow. The model was generated with the program VISP [87].
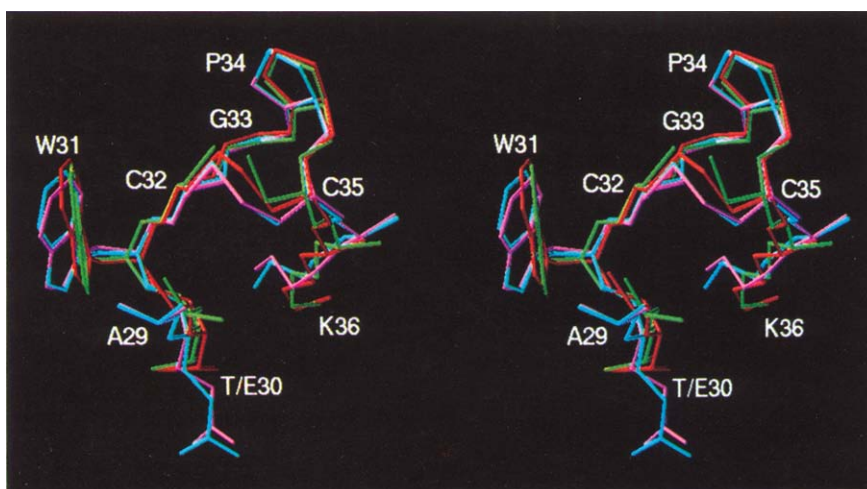
Fig. 11. Best fit superposition of the active site of the restrained minimized mean structures of the reduced and oxidized states of the (C62A, C69A, C73A) mutant of human thioredoxin and the two independent molecules in the X-ray structure of oxidized *E. coli* thioredoxin. The backbone and side chains are shown in green and red for the reduced and oxidized states of human thioredoxin, respectively, and in blue and pink for the two molecules of oxidized *E. coli* thioredoxin. The coordinates of oxidized *E. coli* thioredoxin are from [26].

involvement in filamentous phage assembly, rely on the conformation of the reduced protein, but not its redox function. It is therefore of considerable interest to compare the three-dimensional structures of oxidized and reduced thioredoxin with the aim of understanding its enzymatic function.

In this paper we present high-resolution three-dimensional structures of the reduced and oxidized states of the (C62A, C69A, C73A) mutant of human thioredoxin using multidimensional heteronuclear NMR spectroscopy. The present structures have been determined with high precision and accuracy. As a result, subtle differences between the oxidized and reduced states can be reliably determined. We show that while the global fold of the reduced and oxidized forms of human thioredoxin is very similar, there exist some important localized conformational differences, particularly in the active site region and regions close by. Differences (> 15°) in the ϕ torsion angles of residues Ser28, Ala29, Thr30, Trp31, Cys32, Cys35 and Lys36 and in the ψ angles of residues Ser28, Ala29, Thr30, Pro34, Cys35 and Lys36 are ob-

served between the reduced and oxidized states. These can be attributed to a slight shortening of the C^α–C^α distance by approximately 0.1 Å between Cys32 and Cys35 upon formation of the disulfide bond, and a change in the χ_1 angle of Cys35 from $-50.9 \pm 3.1°$ in the reduced state to $-39.1 \pm 0.7°$ in the oxidized state. A very small difference in the position of the Trp31 side chain in the two states is also observed and is mainly attributable to the changes in backbone torsion angles and a 10° change in the χ_2 angle. The changes in the active site are propagated to the neighboring helices, $\alpha2$ and $\alpha4$, whose orientations with respect to the underlying β-sheet are slightly different in the two states, as well as to the two loops (residues 74–76 and 90–92) that oppose the active site. As a result, the width of the cleft which is formed by the active site and the two opposing loops and which encompasses all known interacting sites on thioredoxin, is increased by about 10 % in the oxidized state relative to the reduced state. Given the close similarity between the active sites of human and *Escherichia coli* thioredoxins, it is possible that the difference in

activity between the reduced and oxidized states with regard to non-redox functions may not be related so much to the small structural differences between the isolated reduced and oxidized states, but rather to their ability to undergo the required conformational changes when interacting with the target protein.

Materials and methods

Sample preparation

The (C62A, C69A, C73A) mutant of human thioredoxin was prepared as described previously [29]. Uniform (>95%) ^{15}N and/or ^{13}C labeling was achieved by growing the bacteria on minimal medium with ^{15}NH$_4$Cl and/or ^{13}C$_6$-glucose as the sole nitrogen and carbon sources, respectively.

Samples of reduced human thioredoxin were prepared by reducing a 1.3 mM solution of ^{15}N and/or ^{15}N/^{13}C-labeled protein with excess dithiothreitol (DTT) at pH 7.0, and dialyzed and concentrated by centrifugation against 100 mM sodium phosphate buffer pH 5.4 with 0.2 mM deuterated DTT. The samples were kept in argon-purged buffer containing either 90 % H$_2$O/10 % D$_2$O or 99.996 % D$_2$O, in NMR tubes sealed with airtight rubber septa. Under these conditions reduced human thioredoxin can remain in a reduced state for $\sim$4 months. This was verified by periodically recording ^{1}H–^{15}N correlation spectra on the samples. The oxidized samples were prepared by stirring a reduced sample at 10 μM concentration in air at 25°C for 10 h to yield a disulfide between the two active-site cysteines and then concentrated to 1.2 mM.

NMR spectroscopy

All NMR spectra reported were recorded at 25°C on Bruker AMX600 and AMX500 spectrometers equipped with a triple-resonance self-shielded z-gradient probe. Quadrature detection in the indirectly detected dimensions was obtained using the TPPI-States method [49]. Spectra were processed using the in-house program nmrPipe (F Delaglio, unpublished program) and analyzed using the interactive software PIPP, CAPP and STAPP ([50] and DS Garrett, unpublished program).

Chemical shift assignments

The sequential assignment of the ^{1}H, ^{13}C and ^{15}N chemical shifts was achieved by means of through-bond heteronuclear correlations along the backbone and side chains (for reviews see [35,51]) using the following series of 3D spectra: HNHA [52], CBCANH [53], CBCACONH [54], HBHACONH [55], C(CO)NH [56], H(CCO)NH [56], HCCH-COSY [57] and HCCH-TOCSY [58] to demonstrate C$^\alpha$H(i)-^{15}N(i)-NH(i), ^{13}C$^\beta$/C$^\alpha$(i)-^{15}N(i)-NH(i) and ^{13}C$^\beta$/C$^\alpha$(i−1)-^{15}N(i)-NH(i), ^{13}C$^\beta$/C$^\alpha$(i−1)-^{15}N(i)-NH(i), C$^\beta$H/C$^\alpha$H(i−1)-^{15}N(i)-NH(i), ^{13}C$_j$(i−1)-^{15}N(i)-NH(i), H$_j$(i−1)-^{15}N(i)-NH(i), H$_j$-^{13}C$_j$-^{13}C$_{j\pm1}$-H$_{j\pm1}$, and H$_j$-^{13}C$_j$-^{13}C$_{j\pm n}$-H$_{j\pm n}$ correlations, respectively (note that i refers to the residue number, and j to the carbon position along a side chain). During the course of this work it became apparent that the ^{15}N and ^{1}H resonance assignments that we had previously reported for the reduced form of the (C62A, C69A, C73A) mutant of human thioredoxin [29] were in fact those of the oxidized form.

Torsion angle restraints and stereospecific assignments

ϕ, ψ, and χ_1 torsion angle restraints and stereospecific β-methylene assignments were derived from $^3J_{HN\alpha}$ and $^3J_{\alpha\beta}$ coupling constants supplemented by intra-residue and sequential inter-residue distances involving the NH, C$^\alpha$H and C$^\beta$H protons us-

ing the conformational grid search program STEREOSEARCH [59]. The sequential inter-residue distances were derived from 3D ^{15}N-separated and ^{13}C-separated ROE experiments (mixing times 35 ms) to circumvent problems arising from spin-diffusion. Quantitative $^3J_{HN\alpha}$ coupling constants, measured to an accuracy of ±0.5 Hz, were obtained from a 3D HNHA experiment [52], and qualitative $^3J_{\alpha\beta}$ coupling constants were derived from a 3D ^{15}N-separated HOHAHA experiment [60]. The stereospecific assignments and the presence of rotamer averaging were also verified from a qualitative assessment of the $^3J_{NH\beta}$ and $^3J_{COH\beta}$ heteronuclear couplings derived from 3D HNHB [61] and HN(CO)HB [62] experiments, respectively. Quantitative heteronuclear $^3J_{C\gamma N}$ and $^3J_{C\gamma CO}$ coupling constants, obtained from 2D ^{13}C-{^{15}N}- and ^{13}C-{^{13}CO}-spin-echo difference constant time heteronuclear single quantum coherence spectra, respectively, were used to determine the χ_1 angles of threonine and valine and stereospecific assignments of valine methyl groups [63,64]. χ_2 restraints for isoleucine and leucine and stereospecific assignments for the methyl groups of leucine were obtained from $^3J_{CC}$ coupling constants and the pattern of intra-residue NOEs [65]. The $^3J_{CC}$ coupling constants were measured from a 2D long-range carbon–carbon correlation spectrum [66]. Stereospecific assignments were obtained for 51 out of the 69 β-methylene groups, and for all 11 valine and 6 leucine methyl groups.

Interproton distance restraints

NOEs between NH protons, between NH and carbon-attached protons, and between carbon-attached protons were assigned from 3D ^{15}N-separated NOE [31], 4D ^{15}N/^{13}C-separated NOE [32] and 4D ^{13}C/^{13}C-separated [33,34] NOE spectra, respectively, recorded with a mixing time 120 ms. The two 4D heteronuclear separated spectra were recorded with two scans per increment and a total measuring time of about 84 h using sinebell shaped pulsed-field gradients to eliminate undesired coherence transfer pathways [67] exactly as described before [34]. The NOEs were classified into strong, medium, weak and very weak categories corresponding to interproton distance restraints of 1.8–2.7 Å (1.8–2.9 Å for NOEs involving NH protons), 1.8–3.3 Å (1.8–3.5 Å for NOEs involving NH protons), 1.8–5.0 Å, and 1.8–6.0 Å, respectively [36,37]. The upper bounds for distances involving methyl protons and non-stereospecifically assigned methylene protons were corrected appropriately for center averaging [68], and an additional 0.5 Å was added to the upper distance limits for NOEs involving methyl protons [69,70].

Hydrogen-bonding restraints

The hydrogen-bonding restraints were deduced on the basis of slowly-exchanging NH protons and the pattern of sequential and inter-strand NOEs involving the NH and C$^\alpha$H protons [71]. Slowly-exchanging NH protons were identified from a series of 2D ^{15}N–^{1}H Overbodenhausen correlation spectra [72,73] acquired over a period of 24 h starting within 5 min of dissolving an unexchanged sample of lyophilized protein in D$_2$O [29,49]. Two distance restraints were used for each hydrogen bond: one (of 1.5–2.3 Å) between the hydrogen and the acceptor atom and one (of 2.4–3.3 Å) between the donor heavy atom and the acceptor atom. These were only introduced after the initial set of structure calculations.

Localization of bound water molecules

Bound water molecules were located on the basis of 2D H$_2$O-NOE/ROE ^{1}H–^{13}C HSQC and H$_2$O-ROE-^{1}H–^{15}N HSQC experiments [43–45] recorded with NOE and ROE mixing times of 100 ms and 60 ms, respectively. We accurately located six and seven bound water molecules in the interior of reduced and oxidized human thioredoxin, respectively. In addition, we observed numerous water molecules at the surface of the protein.

Structure calculations

Structures were calculated using the hybrid distance geometry-dynamical simulated annealing method of Nilges *et al.* [74] with minor modifications [75], making use of the program X-PLOR [76–78]. The target function that is minimized during simulated annealing (as well as during conventional Powell minimization) comprises only quadratic harmonic terms for covalent geometry (that is bonds, angles, planes, and chirality), square-well quadratic potentials for the experimental distance and torsion angle restraints [37], an harmonic potential for the $^3J_{HN\alpha}$ coupling constant restraints [79,80], and a quartic van der Waals repulsion term for the non-bonded contacts [74,81,82]. All peptide bonds were constrained to be planar and *trans*, with the exception of the peptide bond between Thr74 and Pro75 which was constrained to be planar and *cis* on the basis of the NOE data which unambiguously indicated the presence of a *cis*-proline. There were no hydrogen-bonding, electrostatic, or 6–12 Lennard–Jones empirical potential energy terms in the target function.

The coordinates of the simulated annealing structures for the oxidized and reduced forms of the (C62A, C69A, C73A) mutant of human thioredoxin (40 each), together with the corresponding restrained minimized mean coordinates, have been deposited in the Brookhaven Protein Data Bank, together with the complete set of ^1H, ^{13}C and ^{15}N resonance assignments and experimental NMR restraints.

References

1. Holmgren, A. (1985). Thioredoxin. *Annu. Rev. Biochem.* **54**, 237–271.
2. Holmgren, A. (1989). Thioredoxin and glutaredoxin systems. *J. Biol. Chem.* **264**, 13963–13966.
3. Eklund, H., Gleason, F.K. & Holmgren, A. (1991). Structural and functional relations among thioredoxins of different species. *Proteins* **11**, 13–28.
4. Laurent, T.V., Moore, E.C. & Reichard, P. (1964). *J. Biol. Chem.* **239**, 3436–3444.
5. Engstrom, N.E., Holmgren, A., Larsson, A. & Soderhall, S. (1974). Isolation and characterization of calf liver thioredoxin. *J. Biol. Chem.* **249**, 205–210.
6. Buchanan, B.B. (1991). Regulation of CO_2 assimilation in oxygenic photosynthesis: the ferredoxin/thioredoxin system. Perspective on its discovery, present, and future development. *Arch. Biochem. Biophys.* **288**, 1–9.
7. Tagaya, Y., *et al.*, & Yodoi, J. (1989). ATL-derived factor (ADF), and IL-2R/Tac inducer homologous to thioredoxin: possible involvement of dithiol-reduction in the IL-2 receptor induction. *EMBO J.* **8**, 757–764.
8. Wakasugi, N., *et al.*, & Tursz, T. (1990). Adult T-cell leukemia-derived factor/thioredoxin, produced by both human T-lymphotropic virus type I- and Epstein-Barr virus-transformed lymphocytes, acts as an autocrine growth factor and synergizes with interleukin 1 and interleukin 2. *Proc. Natl. Acad. Sci. USA* **87**, 8282–8286.
9. Matthews, J.R., Wakasugi, N., Virelizier, J.L., Yodoi, J. & Hay, R.T. (1992). Thioredoxin regulates the DNA binding activity of NF-κB by reduction of a disulfide bond involving cysteine 62. *Nucleic Acids Res.* **20**, 3821–3830.
10. Hayashi, T., Ueno, Y. & Okamoto, T. (1993). Oxidoreductive regulation of nuclear factor κB. *J. Biol. Chem.* **268**, 11380–11388.
11. Kallis, G.B. & Holmgren, A. (1980). Differential reactivity of the functional sulfhydryl groups of cysteine-32 and cysteine-35 present in the reduced form of thioredoxin from *Echerichia coli. J. Biol. Chem.* **255**, 10261–10265.
12. Holmgren, A. (1972). Tryptophan fluorescence study of conformational transitions of the oxidized and reduced form of thioredoxin. *J. Biol. Chem.* **247**, 1992–1998.
13. Dyson, H.J., Holmgren, A. & Wright, P. E. (1988). Structural differences between oxidized and reduced thioredoxin monitored by two-dimensional ^1H NMR spectroscopy. *FEBS Lett.* **228**, 254–258.
14. Chadrasekhar, K., Krause, G., Holmgren, A. & Dyson, H.J. (1991). Assignment of the ^{15}N NMR spectra of reduced and oxidized *Escherichia coli* thioredoxin *FEBS Lett.* **284**, 178–183.
15. Chandrasekhar, K., Campbell, A. P., Jeng, M.-F., Holmgren, A. & Dyson, H.J. (1994). Effect of disulfide bridge formation on the NMR spectrum of a protein: studies on oxidized and reduced *Echerichia coli* thioredoxin. *J. Biomol. NMR*, in press.
16. Kaminski, S.M. & Richards, F.M. (1992). Differences in hydrogen exchange behaviour between the oxidized and reduced forms of *Escherichia coli* thioredoxin. *Protein Sci.* **1**, 10–21.
17. Kaminski, S.M. & Richards, F.M. (1992). Reduction of thioredoxin significantly decreases its partial specific volume and adiabatic compressibility. *Protein Sci.* **1**, 22–30.
18. Huber, H.E., Russel, M., Model, P. & Richardson, C.C. (1986). Interaction of mutant thioredoxins of *Escherichia coli* with the gene 5 protein of phage T7. The redox capacity of thioredoxin is not required for stimulation of DNA polymerase activity. *J. Biol. Chem.* **261**, 15006–15012.
19. Russel, M. & Model, P. (1986). The role of thioredoxin in filamentous phage assembly. *J. Biol. Chem.* **261**, 14997–15005.
20. Stone, M.J., Chandrasekhar, K., Holmgren, A., Wright, P.E. & Dyson, H.J. (1993). Comparison of backbone and tryptophan side-chain dynamics of reduced and oxidized *Escherichia coli* thioredoxin using ^{15}N NMR relaxation measurements. *Biochemistry* **32**, 426–435.
21. Holmgren, A., Kallis, G.B. & Nordstrom, B. (1981). A mutant thioredoxin from *Escherichia coli* tsnC 7007 that is nonfunctional as subunit of phage T7 DNA polymerase. *J. Biol. Chem.* **256**, 3118–3124.
22. Gleason, F.K., Lim, L.J., Gerami-Nejad, M. & Fuchs, J.A. (1990). Characterization of *Escherichia coli* thioredoxins with altered active site residues. *Biochemistry* **29**, 3701–3709.
23. Krause, G. & Holmgren, A. (1991). Substitution of the conserved tryptophan 31 in *Escherichia coli* thioredoxin by site-directed mutagenesis and structure–function analysis. *J. Biol. Chem.* **266**, 4056–4066.
24. Krause, G., Lundstrom, J., Lopez-Barea, J., Pueyo de La cuesta, C. & Holmgren, A. (1991). Mimicking the active site of protein disulfide isomerase by substitution of proline 34 in *Escherichia coli* thioredoxin. *J. Biol. Chem.* **266**, 9494–9500.
25. Holmgren, A., Söderberg, B.O., Eklund, H. & Branden, C.-I. (1975). Three dimensional structure of *Escherichia coli* thioredoxin-S2 to 2.8Å resolution. *Proc. Natl. Acad. Sci. USA* **72**, 2305–2309.
26. Katti, S.K., LeMaster, D.M. & Eklund, H. (1990). Crystal structure of thioredoxin from *Escherichia coli* at 1.68Å resolution. *J. Mol. Biol.* **212**, 167–184.
27. Dyson, H.J., Gippert, G.P., Case, D.A., Holmgren, A. & Wright, P.E. (1990). Three-dimensional solution structure of the reduced form of *Escherichia coli* thioredoxin determined by nuclear magnetic resonance spectroscopy. *Biochemistry* **29**, 4129–4136.
28. Forman-Kay, J.D., Clore, G.M., Wingfield, P.T. & Gronenborn, A.M. (1991). High-resolution three-dimensional structure of reduced recombinant human thioredoxin in solution. *Biochemistry* **30**, 2685–2698.
29. Forman-Kay, J.D., Clore, G.M., Stahl, S.J. & Gronenborn, A.M. (1992). ^1H and ^{15}N resonance assignments and secondary structure of the human thioredoxin C62A, C69A, C73A mutant. *J. Biomol. NMR.* **2**, 431–445.
30. Marion D., Kay, L.E., Sparks, S.W., Torchia, D.A. & Bax, A. (1989). Three-dimensional heteronuclear NMR of ^{15}N labeled proteins. *J. Am. Chem. Soc.* **111**, 1515–1517.
31. Marion, D., *et al.*, & Clore, G.M. (1989). Overcoming the overlap problem in the assignment of ^1H NMR spectra of larger proteins by use of three-dimensional heteronuclear ^1H–^{15}N Hartmann–Hahn-multiple quantum coherence and nuclear Overhauser-multiple quantum coherence spectroscopy: application to interelukin-1β. *Biochemistry* **28**, 6150–6156.
32. Kay, L.E., Clore, G.M., Bax, A. & Gronenborn, A.M. (1990). Four-dimensional heteronuclear triple-resonance NMR spectroscopy of interleukin-1β in solution. *Science* **249**, 411–414.

33. Clore, G.M., Kay, L.E., Bax, A. & Gronenborn A.M. (1991). Four-dimensional $^{13}C/^{13}C$-edited nuclear Overhauser enhancement spectroscopy of a protein in solution: application to interleukin 1β. *Biochemistry* 30, 12–18.

34. Vuister, G.W., et al., & Bax, A. (1993). Increased resolution and improved spectral quality in four-dimensional $^{13}C/^{13}C$-separated HMQC-NOESY-HMQC spectra using pulsed field gradients. *J. Magn. Reson. B* 101, 210–213.

35. Clore, G.M. & Gronenborn, A.M. (1991). Structures of larger proteins in solution: three- and four-dimensional heteronuclear NMR spectroscopy. *Science* 252, 1390–1399.

36. Williamson, M.P., Havel, T.F. & Wüthrich, K. (1985). Solution conformation of proteinase inhibitor IIA from bull seminal plasma by ^1H nuclear magnetic resonance and distance geometry. *J. Mol. Biol.* 182, 295–315.

37. Clore, G.M., Nilges, M., Sukumaran, D.K., Brünger, A.T., Karplus, M. & Gronenborn, A.M. (1986). The three-dimensional structure of α1-purothionin in solution: combined use of nuclear magnetic resonance, distance geometry and restrained molecular dynamics. *EMBO J.* 5, 2729–2735.

38. Laskowski, R.A., MacArthur, M., Moss, D.S., Thornton, J.M. (1993). PROCHECK: a program to check the stereochemical quality of protein structures. *J. Appl. Crystallogr.* 26, 283–291.

39. Clore, G.M., Robien, M. A. & Gronenborn, A.M. (1993). Exploring the limits of precision and accuracy of protein structures determined by nuclear magnetic resonance spectroscopy. *J. Mol. Biol.* 231, 82–102.

40. Clore, G.M., Brünger, A.T. Karplus, M. & Gronenborn, A.M. (1986). Application of molecular dynamics with interproton distance restraints to three-dimensional protein structure determination: a model study of crambin. *J. Mol. Biol.* 191, 523–551.

41. Brünger, A.T., Clore, G.M., Gronenborn, A.M. Saffrich, R. & Nilges, M. (1993). Assessing the quality of solution nuclear magnetic resonance structures by complete cross-validation. *Science* 261, 328–331.

42. Richardson, J.S. (1981). The anatomy and taxonomy of protein structure. *Adv. Prot. Chem.* 34, 167–339.

43. Forman-Kay, J.D., Clore, G.M. & Gronenborn, A.M. (1992). Relationship between electrostatics and redox function in human thioredoxin: characterization of pH titration shifts using two-dimensional homo- and heteronuclear NMR. *Biochemistry* 31, 3442–3452.

44. Grzesiek, S. & Bax, A. (1993). Measurement of amide proton exchange rates and NOEs with water in $^{13}C/^{15}N$-enriched calcineurin B. *J. Biomol. NMR* 3, 627–638.

45. Grzesiek, S. & Bax, A. (1993). The importance of not saturating H_2O in protein NMR. Application to sensitivity enhancement and NOE measurements. *J. Am. Chem. Soc.* 115, 12593–12594.

46. Clore, G.M., Bax, A., Omichinski, J. & Gronenborn, A.M. (1994). Localization of bound water in the solution structure of a complex of the erythroid transcription factor GATA-1 with DNA. *Structure* 2, 89–94.

47. Forman-Kay, J.D., Gronenborn, A.M., Wingfield, P.T. & Clore, G.M. (1991). Determination of the positions of bound water molecules in the solution structure of reduced human thioredoxin by heteronuclear three-dimensional nuclear magnetic resonance spectroscopy. *J. Mol. Biol.* 220, 209–216.

48. Otting, G., Liepinsh, E. & Wüthrich, K. (1991). Protein hydration in aqueous solution. *Science* 254, 974–980.

49. Marion, D., Ikura, M., Tschudin, R. & Bax, A. (1989). Rapid recording of 2D NMR spectra without phase cycling: application to the study of hydrogen exchange in proteins. *J. Magn. Reson.* 85, 393–399.

50. Garrett, D.S., Powers, R., Gronenborn, A.M., & Clore, G.M. (1991). A common-sense approach to peak picking in two- three- and four-dimensional spectra using automatic computer analysis of contour diagrams. *J. Magn. Reson.* 95, 214–220.

51. Bax, A. & Grzesiek, S. (1993). Methodological advances in protein NMR. *Accounts Chem. Res.* 26, 131–138.

52. Vuister, G.W. & Bax, A. (1993). Quantitative J correlation: a new approach for measuring homonuclear three-bond J(H^NH^α) coupling constants in ^{15}N-enriched proteins. *J. Am. Chem. Soc.* 115, 7772–7777.

53. Grzesiek, S. & Bax, A. (1992). An efficient experiment for sequential backbone assignment of medium-sized isotopically enriched proteins. *J. Magn. Reson.* 99, 201–207.

54. Grzesiek, S. & Bax, A. (1992). Correlating backbone amide and side chain resonances in larger proteins by multiple relayed triple resonance NMR. *J. Am. Chem. Soc.* 114, 6291–6293.

55. Grzesiek, S. & Bax, A. (1993). Amino acid type determination in the sequential assignment procedure of uniformly $^{13}C/^{15}N$-enriched proteins. *J. Biomol. NMR* 3, 185–204.

56. Grzesiek, S., Anglister, J. & Bax, A. (1993). Correlation of backbone amide and aliphatic side-chain resonances in $^{13}C/^{15}N$-enriched proteins by isotropic mixing of ^{13}C magnetization. *J. Magn. Reson. B* 101, 114–119.

57. Bax, A., Clore, G.M., Driscoll, P.C., Gronenborn, A.M., Ikura, M. & Kay, L.E. (1990). Practical aspects of proton-carbon-carbon-proton three-dimensional correlation spectroscopy of ^{13}C-labeled proteins. *J. Magn. Reson.* 87, 620–627.

58. Bax, A., Clore, G.M. & Gronenborn, A.M. (1990). $^1H–^1H$ correlation via isotropic mixing of ^{13}C magnetization, a new three-dimensional approach for assigning ^1H and ^{13}C spectra of ^{13}C-enriched proteins. *J. Magn. Reson.* 88, 425–431.

59. Nilges M., Clore, G.M. & Gronenborn, A.M. (1990). ^1H-NMR stereospecific assignments by conformational data-base searches. *Biopolymers* 29, 813–822.

60. Clore, G.M., Bax, A. & Gronenborn, A.M. (1991). Stereospecific assignment of β-methylene protons in larger proteins using 3D ^{15}N-separated Hartmann–Hahn and ^{13}C-separated rotating frame Overhauser spectroscopy. *J. Biomol. NMR* 1, 13–22.

61. Archer, S.J., Ikura, M., Torchia, D.A. & Bax, A. (1991). An alternative 3D NMR technique for correlating backbone ^{15}N with side chain Hβ resonances in larger proteins. *J. Magn. Reson.* 95, 636–641.

62. Grzesiek, S., Ikura, M., Clore, G.M., Gronenborn, A.M., & Bax, A. (1992). A 3D triple-resonance NMR technique for qualitative measurement of carbonyl-Hβ J couplings in isotopically enriched proteins. *J. Magn. Reson.* 96, 215–221.

63. Vuister, G.W., Wang, A.C. & Bax, A. (1993). A Measurement of three-bond nitrogen-carbon J couplings in proteins uniformly enriched in ^{15}N and ^{13}C. *J. Am. Chem. Soc.* 115, 5334–5335.

64. Grzesiek, S., Vuister, G.W. & Bax, A. (1993). A simple and sensitive experiment for measurement of J_{CC} couplings between backbone carbonyl and methyl carbons in isotopically enriched proteins. *J. Biomol. NMR* 3, 487.

65. Powers, R., Garrett, D.S., March, C.J., Frieden, E.A. Gronenborn, A.M. & Clore, G.M. (1993). The high resolution structure of human interleukin-4 determined by multidimensional heteronuclear magnetic resonance spectroscopy. *Biochemistry* 32, 6744–6762.

66. Bax, A., Max, D. & Zax, D. (1992). Measurement of multiple-bond $^{13}C–^{13}C$ J couplings in a 20 kDa protein–peptide complex. *J. Am. Chem. Soc.* 114, 6923–6924.

67. Bax, A. & Pochapsky, S.S. (1992). Optimizing recording of heteronuclear multidimensional NMR spectra using pulsed field gradients. *J. Magn. Reson.* 99, 638–643.

68. Wüthrich, K., Billeter, M. & Braun, W. (1983). Pseudo-structures for the 20 common amino acids for use in studies of protein conformations by measurements of intramolecular proton–proton distance constraints with nuclear magnetic resonance. *J. Mol. Biol.* 169, 949–961.

69. Clore, G.M., Gronenborn, A.M., Nilges, M. & Ryan, C.A. (1987). Three-dimensional structure of potato carboxypeptidase inhibitor in solution. A study using nuclear magnetic resonance, distance geometry, and restrained molecular dynamics. *Biochemistry* 26, 8012–8023.

70. Wagner, G., Braun, W., Havel, T.F., Schaumann, T., Go, N. & Wüthrich, K. (1987). Protein structures in solution by nuclear magnetic resonance and distance geometry. The polypeptide fold of the basic pancreatic trypsin inhibitor is determined using two different algorithms, DISGEO and DISMAN. *J. Mol. Biol.* 196, 611–639.

71. Wüthrich, K. (1986). *NMR of Proteins and Nucleic acids*. John Wiley & Sons, New York.

72. Bax, A., Ikura, M., Kay, L.E., Torchia, D.A. & Tschudin, R. (1990). Comparison of different modes of two-dimensional reverse-correlation NMR for the study of proteins. *J. Magn. Reson.* 86, 304–318.

73. Norwood, T.J., Boyd, J., Heritage, J.E., Soffe, N. & Campbell, I.D. (1990). Comparison of techniques for ^1H-detected heteronuclear $^1H–^{15}N$ spectroscopy. *J. Magn. Reson.* 87, 488–501.

74. Nilges, M., Clore, G.M. & Gronenborn, A.M. (1988). Determination of three-dimensional structures of proteins from interproton distance data by hybrid distance geometry-dynamical simulated annealing calculations. *FEBS Lett.* **229**, 317–324.

75. Clore, G.M., Appella, E., Yamada, M., Matsushima, K. & Gronenborn, A.M. (1990). Three dimensional structure of interleukin-8 in solution. *Biochemistry* **29**, 1689–1696.

76. Brünger, A.T., Clore, G.M., Gronenborn, A.M. & Karplus, M. (1986). Three-dimensional structure of proteins determined by molecular dynamics with interproton distance restraints: application to crambin. *Proc. Natl. Acad. Sci. USA* **83**, 3801–3805.

77. Brünger, A.T. (1992). *X-PLOR Version 3.0 Manual.* Yale University, New Haven, CT.

78. Kuszewski, J., Nilges, M. & Brünger, A.T. (1992). Sampling and efficiency of metric matrix distance geometry: a novel partial metrization algorithm. *J. Biomol. NMR* **2**, 33–56.

79. Garrett, D.S., Kuszewski, J., Hancock, T., Vuister, G.W., Gronenborn, A.M. & Clore, G.M. (1994). The impact of direct refinement against three-bond HN-C$^\alpha$coupling constants on protein structure determination by NMR. *J. Magn. Reson.*, in press.

80. Lodi, P.J., *et al.*, & Clore, G.M. (1994). High-resolution solution structure of the β chemokine hMIP-1β by multidimensional NMR. *Science* **263**, 1762–1767.

81. Nilges, M., Gronenborn, A.M., Brünger, A.T. & Clore, G.M. (1988). Determination of three-dimensional structures of proteins by simulated annealing with interproton distance restraints. Application to crambin, potato carboxypeptidase inhibitor and barley serine proteinase inhibitor 2. *Protein Eng.* **2**, 27–38.

82. Nilges, M., Clore, G.M. & Gronenborn, A.M. (1988). Determination of three-dimensional structures of proteins from interproton distance data by dynamical simulated annealing from a random array of atoms. Circumventing problems associated with folding. *FEBS Lett.* **239**, 129–136.

83. Brooks, B.R., Bruccoleri, R.E., Olafson, B.D., States, D.J., Swaminathan, S. & Karplus, M. (1983). CHARMM: a program for macromolecular energy minimization and dynamics calculations. *J. Comput. Chem.* **4**, 187–217.

84. Reiher, W.E. (1985). Theoretical studies of hydrogen bonding [PhD Thesis]. Harvard University, Cambridge, MA, USA.

85. Eisenberg, D. & McLaghlan, A.D. (1986). Solvation energy in protein folding and binding. *Nature* **319**, 199–203.

86. Brünger, A.T. & DeLano, W. (1992). *AVSXPLOR User Manual.* Yale University, New Haven, CT, USA.

87. de Castro, E. & Edelstein, S. (1992). *Visp 1.0 User's Guide.* University of Geneva, Switzerland.

88. Ikura, M., Kay, L.E., Krinks, M. & Bax, A. (1991). A triple resonance NMR study of calmodulin complexed with the binding domain of skeletal muscle myosin light chain kinase: indication of a conformational change in the central helix. *Biochemistry* **30**, 5498–5504.